Modelling of static aerodynamics of helicopter underslung loads

D. I. Greenwell
d.greenwell@city.ac.uk
Centre for Aeronautics
City University
London, UK

ABSTRACT

The complex aerodynamics of rectangular underslung helicopter loads can lead to severe stability problems, but are difficult to represent in flight dynamics models. Current models for box aerodynamics are highly unsatisfactory, being entirely empirical and requiring large amounts of experimental data to generate. This paper presents a new modelling approach, which takes account of the bluff-body nature of the flow, where loads are dominated by normal pressure forces. Existing experimental data is recast in body-axes form, with α and β replaced by velocity components perpendicular and parallel to the box faces. Force and moment data for a wide range of boxes then collapse onto a set of simple generic characteristics, with features that can be related directly to the underlying flow physics. Modelling of container aerodynamics is greatly simplified, and allowance for effects of turbulence, Reynolds Number, wind tunnel interference and geometry modifications becomes possible.

NOMENCLATURE

A_x, A_y, A_z	front, side and top face areas
C_X^*	body-axis axial force component, based on front face area
C_Y^*	body-axis sideforce component, based on side face area
C_Y^*	body-axis normal force component, based on top face area
C_{RM}^*	body-axis rolling moment component, based on side face area and length
C_{PM}^*	body-axis pitching moment component, based on top face area and length
C_{YM}^*	body-axis yawing moment component, based on side face area and length
C_D,C_d	wind-axis drag coefficient, based on projected frontal area
C_L,C_l	wind-axis lift coeficient, based on projected frontal area
C_m	wind-axis pitching moment coefficient, based on projected frontal area and depth
C_{pB}	base pressure coefficient
C_{pmax}	maximum bubble suction pressure coefficient
D	box depth (crossflow dimension)
D_f	projected box depth, = D Cosα + L Sinα,
L	box length (streamwise dimension)
q	dynamic pressure, = ½ρV^2
S	separation bubble length
u,v,w	Cartesian velocity components
V	freestream velocity
W	box width (crossflow dimension)
x,y,z	Cartesian co-ordinates
α	angle of attack, = Tan^{-1}(w/u)
α_R	bubble reattachment incidence
β	sideslip angle, = Sin^{-1}(v/V)
θ, ψ	Euler pitch and yaw angles
ϕ^*	front face crossflow angle, = Tan^{-1}(w/v)
θ^*	side face crossflow angle, = Tan^{-1}(w/u) ≡ α
ψ^*	top face crossflow angle, = Tan^{-1}(v/u)

Paper No. 3577. Manuscript received 13 May 2010, revised version received 9 September 2010, accepted 23 September 2010.
A version of this paper was first presented at The CEAS 2009 European Air and Space Conference, November 2009.

Figure 1. Blackhawk with CONEX underslung load[4].

1.0 INTRODUCTION

An important but hazardous aspect of military & civil helicopter operations is the carrying of underslung loads. For many loads, the maximum speed at which they may be carried is limited not by the available power, but by the (often sudden) onset of instabilities. Three basic types of instability[1] can occur:

1. Aerodynamic instability of the load
2. Helicopter and load vertical oscillations
3. Sling cable flapping

which can force the helicopter pilot to reduce speed quickly, or to jettison the load. For aerodynamic instabilities, the initial load motion is typically a periodic yaw oscillation which then couples into the sling and helicopter response, leading to a range of rather complex lateral and longitudinal pendulum modes. Rectangular box loads are particularly susceptible to aerodynamic instabilities, especially when lightly loaded[2]. Common examples of rectangular loads which have experienced problems are the US Army's 8ft × 6ft × 6ft CONEX (Fig. 1) and 8ft × 8ft × 20ft MILVAN cargo containers.

Considerable effort has been put into the simulation of underslung load instabilities, with various authors developing increasingly sophisticated models of the system dynamics. Stuckey[3] gives a useful review of the field up till 2001; current research groups working in this field include NASA Ames (with Northern Arizona University)[4], Delft University[5], Liverpool University[6] and Aalborg University[7].

For the specific case of aerodynamic instabilities, it is clearly important to model both the static and dynamic aerodynamic characteristics of the load. However, constructing adequate aerodynamic models of rectangular box loads for simulation purposes has proven rather difficult, since the large-scale separated flows typical of these bluff bodies lead to highly non-linear and time-dependent aerodynamic characteristics. As a consequence, models rely heavily on experimental data (although some limited progress is being made now on CFD predictions of load aerodynamics[8]).

Unfortunately, obtaining good quality experimental data is also difficult, because:

- achieving the necessary wide range of angle-of-attack (> ±40°) and sideslip (±180°) in a conventional wind tunnel is often not possible due to physical constraints on model mounting arrangements, leading to a need for extrapolation from a limited $\alpha\beta$ incidence domain[9],
- robust model support systems are needed, leading to very high levels of interference, which cannot be accounted for using conventional 'attached flow' tares[9],
- Reynolds Number and turbulence effects on bluff-body aerodynamics are still poorly understood, particularly for 3D flows[10],
- dynamic testing of bluff bodies requires specialized rigs and data analysis techniques[11], and
- the combination of separated flow and large-amplitude motion means that, unlike conventional aircraft, there is no simple theoretical analysis for the characteristics of a rectangular box upon which to build an aerodynamic model.

Current 'static' aerodynamic models are therefore largely based on empirical representations of wind-tunnel data from small-scale tests, with extrapolation rules based on geometric symmetry considerations. The sophistication of these models varies widely, covering:

- linearised (small-amplitude) stability derivatives[12],
- derivatives augmented by geometric factors for large pitch/yaw angles[5],
- empirical fits to large-amplitude tunnel data[13],
- comprehensive look-up tables [14].

Dynamic wind tunnel test data for 3D box loads is very limited, and rather inconsistent, so many models do not include any dynamic effects at all. Those that do again use a range of techniques, with varying degrees of success:

- simple damping terms[13],
- conventional dynamic derivatives[15],
- transfer function fits to frequency-dependent derivatives [16,17].

The current situation for modelling rectangular box static and dynamic aerodynamics is highly unsatisfactory. Models used are essentially empirical, requiring large amounts of wind tunnel (or CFD) data to generate, and providing no rational basis for correction of Reynolds Number, free-stream turbulence, and support interference effects. These models give no insight into the underlying flow physics, and do not provide any means for prediction of the aerodynamic characteristics of new (or modified) load geometries. Many studies have used only simple drag models, so missing any rotational components of the load aerodynamics.

As a first step to addressing these problems, this paper presents an alternative approach to static modelling of rectangular loads, based on the use of

a. a more appropriate form for the basic aerodynamic model structure, and
b. the partition of the characteristics into elements related to readily identifiable features of the basic bluff-body flow.

By establishing a physical foundation for a static aerodynamic model, data scaling, correction and extrapolation can be put on a more rigorous footing. In turn, this approach then provides an improved starting point for the inclusion of unsteady dynamic effects.
The model development will proceed in incremental stages:

- a review of the basic features of separated flows on 2D rectangular prisms
- identification of relationships between the flow topology and aerodynamic loads as incidence is varied
- a comparison of 2D and 3D rectangular box aerodynamics for planar (pitch or yaw) motion
- a review of the effect of non-planar motion (combined pitch and yaw)

https://doi.org/10.1017/S0001924000005650 Published online by Cambridge University Press

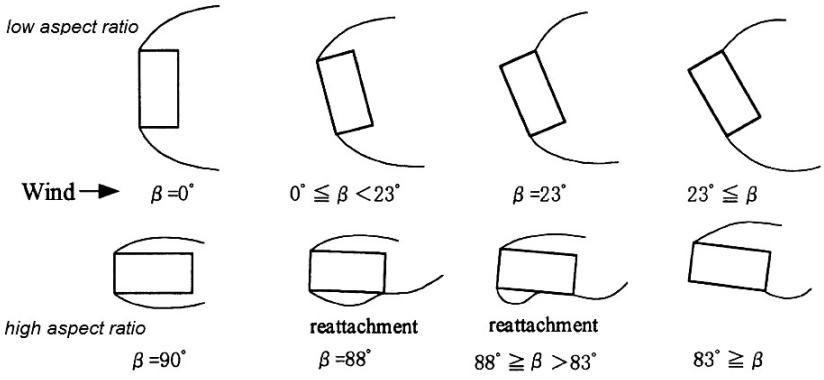

Figure 2. Effect of incidence angle on flow separation & reattachment[19].

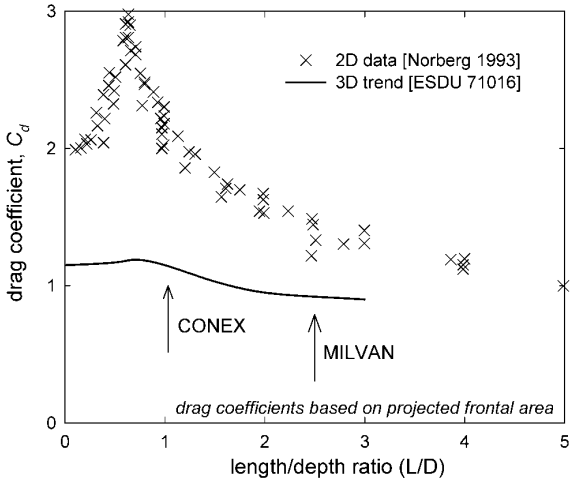

Figure 3. Effect of aspect ratio on drag[10,18].

- a proposal for an alternative set of incidence angles for large-amplitude motion with separated flow, leading on to
- development of a generic six-degree-of-freedom aerodynamic model for rectangular boxes

2.0 2D AERODYNAMICS OF RECTANGULAR PRISMS

2.1 General features

The basic features of separated flows on 3D rectangular containers are similar to those found on 2D rectangular prisms, which have been the subject of extensive experimental investigation[18] because of their relevance to slender structures (bridges and tall buildings). As sharp-edged bluff bodies, the flows are dominated by separations from the corners. Which corner the flow separates from depends on (a) the incidence angle (angle of attack and/or sideslip) and (b) the aspect ratio, as shown schematically in Fig. 2[19]. In general, the flow separates from the upstream corners, and for high aspect ratio prisms may then reattach along the sides. As incidence varies, the reattachment points move forward on the windward side, and aft on the leeward side.

The basic geometric parameter for a 2D rectangular prism is the aspect ratio, or length/depth ratio *L/D*. (NB Terminology on bluff-body aerodynamics is rather inconsistent – for example some industrial aerodynamicists refer to this parameter as the height/depth ratio *H/D*. The notation *L/D* is retained to maximise consistency with published work and with 3D geometry definitions; it should not be confused with lift/drag ratio. Flow incidence angle in the literature is variously angle of attack α, sideslip angle β and yaw angle ψ; in this paper the term 'incidence angle' and symbol α will be used for 2D cases).

Figure 3 (redrawn from Refs 10 and 18 shows the variation of drag coefficient (based on frontal area) with length/depth ratio *L/D* for 2D[18] and 3D[10] shapes. There is a very distinct change in drag behaviour at a critical aspect ratio of around 0.6, although this is much less marked for 3D boxes. As aspect ratio is increased, the separation topology changes from a flat-plate-like flow at $L/D <$ 0.6 to a more complex flow with separation at the upwind corners, and a small recirculation zone on the side close to the front[20].

Increasing turbulence (such as that found in the wake of a helicopter rotor) tends to reduce the critical aspect ratio, from 0.6 at normal wind tunnel test conditions to zero for turbulence intensities above around 16%[21]. Typical rectangular box loads lie above the critical aspect ratio (Fig. 3), which helps to simplify the modelling task. Another critical point occurs at an *L/D* of 2·5-3, when the shear layer shed from the front corner re-attaches to the side to form a closed separation bubble. This has no discernible effect on drag, but does correspond to a four-fold increase in the wake Strouhal Number[18] as the wake width suddenly reduces.

The position of the reattachment point has a dominant effect on the aerodynamic characteristics of rectangular prisms at an angle to the flow. For example, Fig. 3[18] shows the variation of lift, drag and pitching moment with incidence angle varying from 0 to 90° for four prisms of aspect ratio 1·0, 1·62, 2·5 and 3 (note that B/A ≡ *L/D* in Ref. 18). The corresponding aerodynamic characteristics for aspect ratios of 0·62, 0·4 and 0·33 (= 1/1·62, 1/2·5 and 1/3) can be obtained by taking 90° as zero incidence.

Note that the reference length used in these 2D coefficients is the projected frontal depth $D_f = D.\text{Cos}\alpha + L.\text{Sin}\alpha$, which varies with incidence. The moment reference centre is the centroid of the prism. For each shape, the incidence angle for which the side face attachment point is at the rear corner is denoted by α_R. Figure 4 clearly shows that this incidence corresponds directly to a break in all three coefficients – lift, drag and pitching moment.

From an aeronautical point of view, the effect of incidence angle is rather counter-intuitive. The lift-curve slope for all aspect ratios below three is negative for low incidences; in slender structures this can lead to a cross-wind 'galloping' instability, as aerodynamic damping becomes negative. The drag initially reduces with increasing incidence (although a part of this behaviour in Fig. 3 is due to the change in projected fron tal area). All aspect ratios are statically stable in pitch at incidences near 0° and 90°, and unstable at 45° (although the difference between shapes is again exaggerated by the use of projected height).

https://doi.org/10.1017/S0001924000005650 Published online by Cambridge University Press

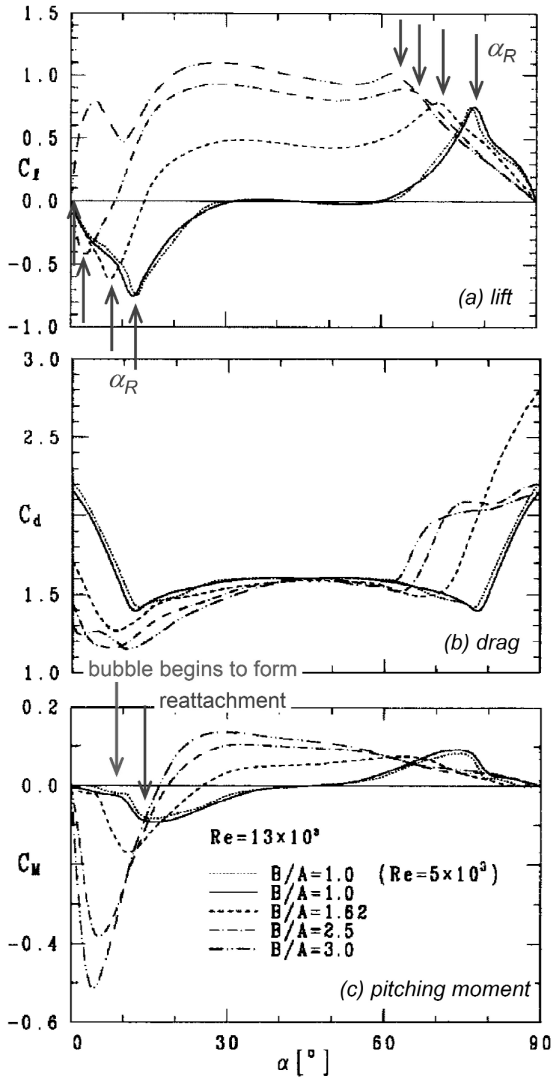

Figure 4. Effect of bubble formation on 2D lift, drag and moment[18] (wind-axis coefficients based on projected depth, *B*/*A* = aspect ratio).

The reasons for this behaviour become apparent when the corresponding side face pressures are examined. For example, Fig. 5 shows the pressure distribution on the windward (lower) side face of a square prism for incidence angles from 0° to 45° [22] (note that in Ref. 22) $S/B \equiv x/L$). At zero incidence (face aligned with the freestream) the flow is fully separated, with an almost flat pressure distribution. By 15° the flow has reattached at the trailing edge (see Figure 1) and a classic separation bubble distribution has formed. The overall suction levels remain very high, leading to the negative lift-curve slope seen in Figure 3. The centre of pressure has shifted forward, leading to a negative (stabilising) pitching moment contribution. The base pressure has risen significantly, leading to a drop in drag.

As incidence is increased past 15°, the attachment point moves forward (Figs 2) towards the leading edge, until at 45° the flow is essentially fully attached. The overall suction levels reduce, contributing to a change in lift from negative to positive. The centre of pressure moves aft, now giving a positive (destabilising) pitching moment contribution. The base pressure remains roughly constant, as does the drag.

The corresponding upper and rear face flows remain fully separated, giving roughly constant pressure distributions. The front face pressures are positive in the region of the stagnation point, which shifts downwards as incidence increases (giving a small negative pitching moment contribution).

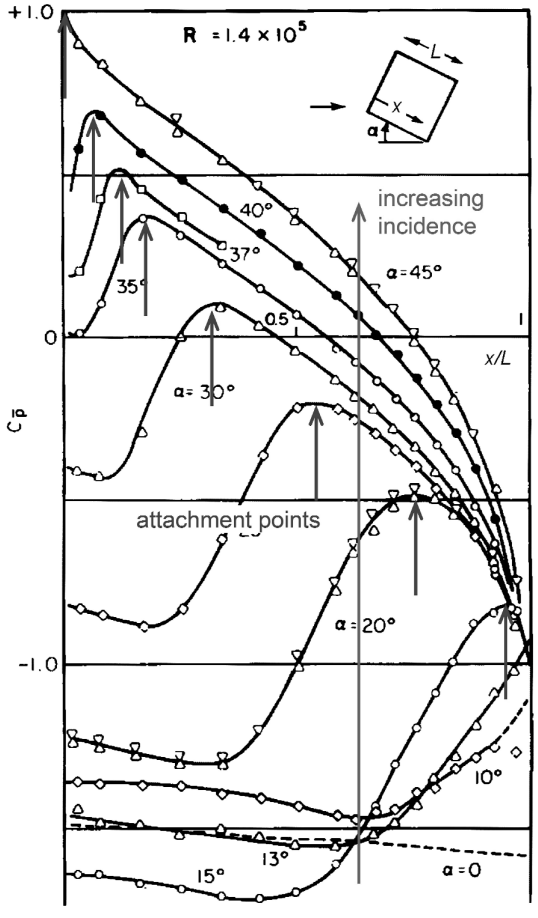

Figure 5. Effect of incidence angle on side face pressure distribution (*L* = prism length, *x* = chordwise position)[22].

2.2 Scaling of 2D pressure distributions

Given the significance of the separation bubble contribution to the aerodynamic characteristics of rectangular prisms, it is important to understand how it is affected by geometry and incidence.

The pressure distributions in Fig. 5 can be split into two elements[22] – a separation bubble of length *S* (taken from the leading-edge to the attachment point), superimposed on an 'attached flow' which varies from +1 at the leading edge to the base-pressure at the trailing-edge of the face. An empirical curve fit to the incidence-dependent 'attached flow' component is developed in Appendix A.

Figure 6 (modified from Ref. 22) demonstrates that for a square prism the bubble component for a range of incidences (from 15° to 35°) can be collapsed onto a single distribution by using the bubble length *S* as a length scale, and the pressure coefficient at the rear of the bubble as a pressure scale.

The same scaling can also be seen in Fig. 7 (modified from Ref. 23) for a range of aspect ratios (L/D = 0·5 to 2·0), at an incidence angle of 20°. What is also evident from Fig. 7 is that the underlying 'attached flow' pressure distribution is independent of aspect ratio. The same is true of the upper (leeward) surface pressures (except for the sub-critical prism 'A', with $L/D < 0{\cdot}6$).

Finally, Figure 8 shows that the variation of the attachment point location S with incidence angle for a range of 2D prisms[18,19,22,23,24] can be collapsed onto a single curve, if the depth *D* is used as a length scale. S/D varies from ~3 at 0° to 0 (fully attached) at 45°. The single 3D dataset available (for a 1:1:2.5 MILVAN container model[11]) shows a similar variation, but with the attachment point much further forward at zero incidence.

https://doi.org/10.1017/S0001924000005650 Published online by Cambridge University Press

To summarise:

- the side face pressure distribution can be split into a separation bubble superimposed on an 'attached' flow
- the attached flow component varies gradually with incidence (Figs 5 and A1), but is independent of aspect ratio (Fig. 7)
- the non-dimensional attachment point *S/D* is a function of incidence only (Fig. 8)
- the magnitude of the separation bubble component is a function only of the 'attached' pressure at the attachment point (Fig. 6).

2.3 Effect on forces and moments

The surface pressures on one face of a rectangular prism can be integrated to give the mean pressure coefficient (= normal force coefficient based on face area) and moment coefficient (about the mid-face, based on face length *L* or *D*) as a function of incidence. Figure 9 shows such an integration for a square prism (based on data in Refs 22 and 10.

The incidence angle convention here is that of ESDU 71016[10], with 0° and 180° corresponding to an orientation perpendicular to the flow, at the front of the prism and rear of the prism respectively. An incidence angle of 90° therefore corresponds to a face oriented parallel to the flow, at the upper side of the prism. The pressure curve is symmetric about 0°, and the moment curve is antisymmetric.

Starting at 0°, the face is perpendicular to the oncoming flow, with the stagnation point in the centre giving zero moment and a mean pressure coefficient of the order of +0·7. As pitch angle is increased the face moves upwards and away from the flow. The mean pressure begins to reduce, and the stagnation point moves downwards (Fig. A1), giving a negative (stabilising) moment contribution. At 45° the stagnation point has moved to the front corner, with the pressure on the face varying almost linearly from +1 at the leading-edge to the base-pressure at the trailing edge (Fig. 4). The mean pressure is close to zero, while the moment has reached its maximum negative value.

As incidence is increased from 45°, the flow separates at the front corner, and a separation bubble forms. The mean pressure continues to decrease smoothly. The localised high suction under the separation bubble at the leading-edge of the face (Fig. 5) gives a positive (destabilising) moment contribution, and the moment curve abruptly reverses. As pitch angle increases the separation bubble grows longer and longer, giving an increasingly negative mean pressure and a moment coefficient changing sign from negative to positive.

Eventually the attachment point reaches the rear of the face (in this case for $S/L = 1$ at about 90°−15° = 75° from Fig. 8), and the bubble breaks down into a fully separated flow by 90°. The pitching moment drops to near zero, while the mean pressure begins to rise slightly. From 90° to 180° the mean (base) pressure remains almost constant, at a value which depends on the aspect ratio *L/D* (Fig. 3). The moment coefficient becomes slightly negative, and then comes back to zero at 180°.

From the discussion in Section 2.2, rectangular prisms of higher aspect ratios should behave in a similar manner to Fig. 9, with two exceptions. The base pressure at 180° is (less negative), giving lower overall drag (Fig. 3), and the reattachment incidence α_R is delayed (eg to 90° for a 3:1 aspect ratio, Fig. 8).

2.4 Simplified modelling

The variation in normal force and moment for a single face discussed above can be used to build up a generic model of the corresponding lift, drag and pitching moment for a complete rectangular prism, combining the contributions from all four faces as incidence is varied. There is insufficient experimental data available to fully develop this model, but it is useful in illustrating the relative impact of the attached and separated flow contributions.

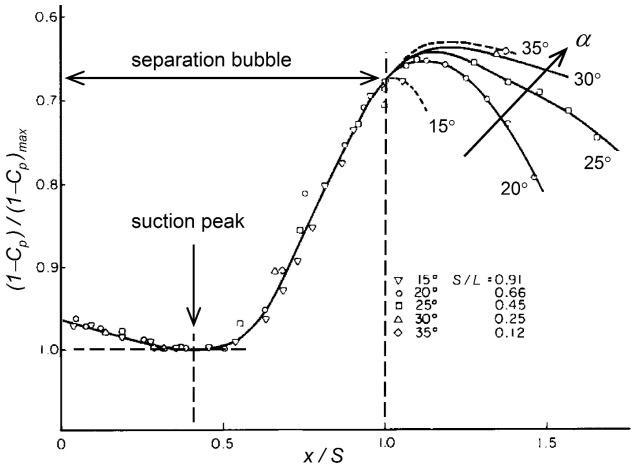

Figure 6. Collapse of separation bubble pressure distribution[22] for a square prism.

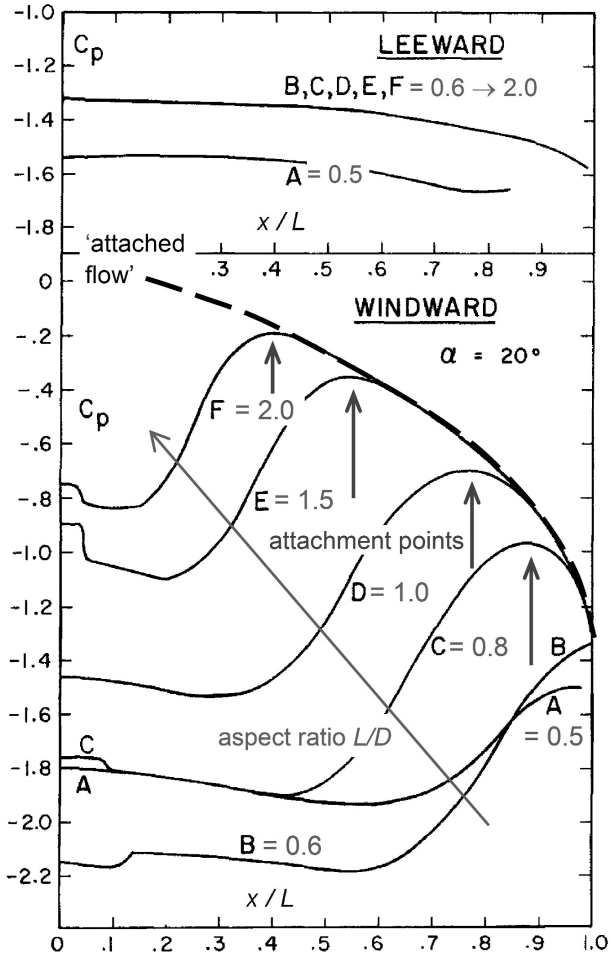

Figure 7. Effect of aspect ratio (*L/D*) on side face pressure distributions at 20° incidence[23].

https://doi.org/10.1017/S0001924000005650 Published online by Cambridge University Press

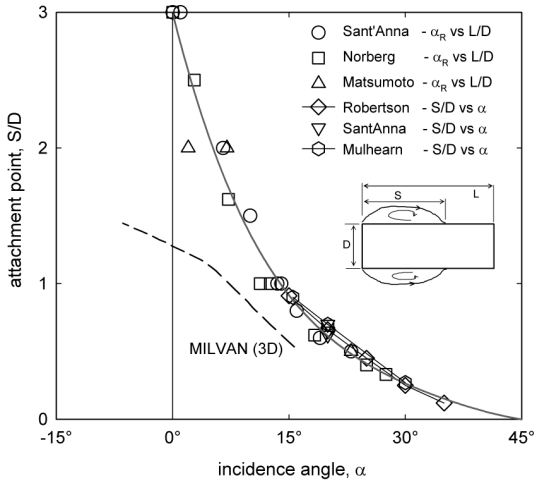

Figure 8. Universal scaling of 2D attachment point.

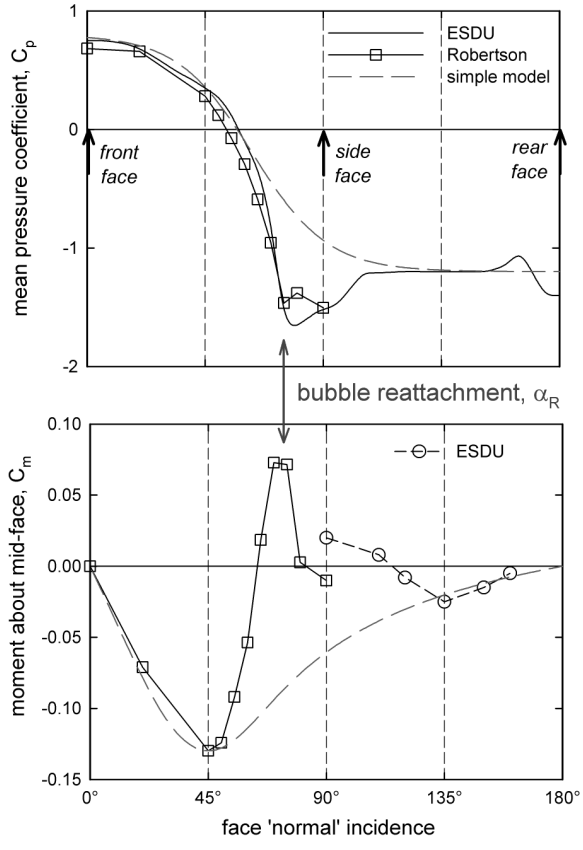

Figure 9. Effect of inclination on mean pressure and moment about mid-face for a square 2D prism[10,22].

The dashed line in Fig. 9 is a modified exponential fit to the underlying 'attached flow' contribution (Appendix A), extended to cover the full incidence range. For the purposes of a preliminary analysis the superimposed 'separated flow' contribution can then be represented by a piecewise linear fit between 45° and 135°, with the location of the maximum value given by the reattachment incidence from Fig. 8.

Combining the contributions from opposing faces then gives the normal force coefficient (upper and lower faces) and axial force coefficient (front and rear faces). For example, Fig. 10 shows these components for a 3:1 prism.

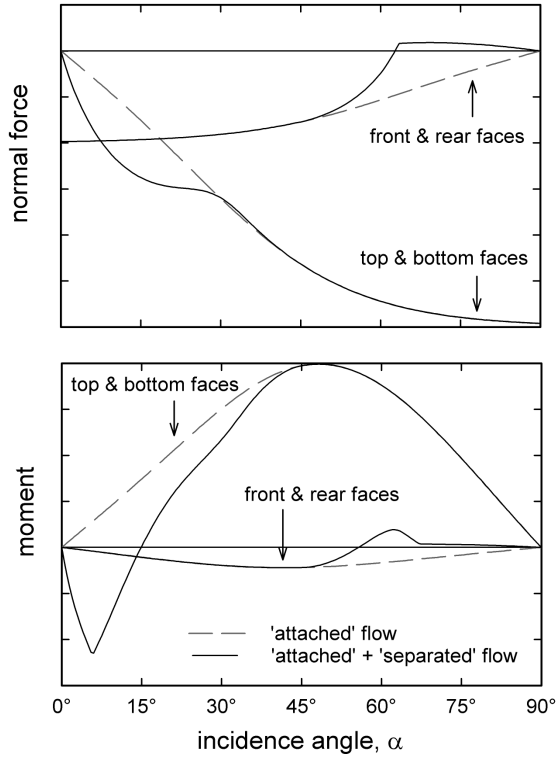

Figure 10. Modelled contributions from opposing faces to forces and moments on a 3:1 prism.

Figure 11 shows results from the same model for a range of aspect ratios, but with the axial force and normal force combined into conventional lift and drag coefficients. The projected frontal depth D_f has been used as the reference length, in order to permit a direct comparison with the experimental data of Fig. 4. The 'attached flow' contribution to the 3:1 prism is indicated by the dashed line. A comparison of Fig. 4 and Fig. 11 clearly demonstrate that this approach captures the basic behaviour of 2D rectangular prisms.

It is also clear that this is not a useful way of presenting the aerodynamic coefficients of a bluff body. The variation in reference length D_f with incidence obscures the basic aerodynamic behaviour, while conventional wind-axis lift and drag coefficients are not appropriate for a rectangular bluff body.

In this case, with large-scale separated flow, the normal pressure loads on each face are much larger than the tangential forces, and so body-axis axial and normal force coefficients would correspond more closely to the underlying flow physics. The effectiveness of this alternative approach is shown in Fig. 12(a), which redraws data from Fig. 4[18] as body-axis coefficients based on the corresponding side lengths (denoted by a superscript*). The usual aeronautical sign conventions are applied.

The normal force coefficients C_Z^* are based on the upper and lower side length L (with equivalent L/D = 1, 1·62, 2·5 and 3) and plotted *vs* incidence α. The axial force coefficients C_X^* are based on the front and rear side depth D (with equivalent L/D = 0·33, 0·4, 0·62 and 1), and plotted *vs* 90°–α to give direct comparison with the normal force. Also shown for comparison is the normal force coefficient for a NACA 0012 aerofoil[25] for normal (leading-edge forward) and reversed (trailing-edge forward) orientations.

The normal force coefficients converge to a limiting sine curve (similar to that seen in Fig. 10) of;

$$C_Z^* \approx -1{\cdot}9\mathrm{Sin}\alpha - 0{\cdot}35\mathrm{Sin}2\alpha$$

$$C_X^* \approx -1{\cdot}9\mathrm{Sin}\left(90^\circ - \alpha\right) - 0{\cdot}35\mathrm{Sin}\left(180^\circ - 2\alpha\right) = -1{\cdot}9\mathrm{Cos}\alpha - 0{\cdot}35\mathrm{Sin}2\alpha \quad \ldots (1)$$

https://doi.org/10.1017/S0001924000005650 Published online by Cambridge University Press

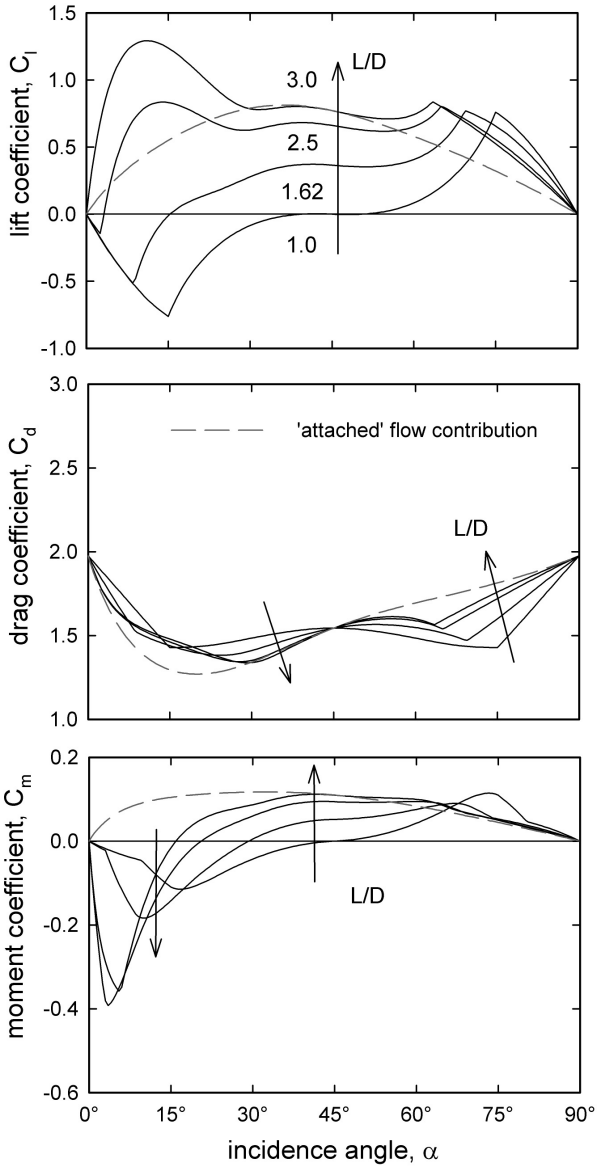

Figure 11. Modelled effect of *L/D* on 2D prism lift, drag and moment (coefficients as Fig. 4).

At low incidences the increased suction due to the separation bubble on the lower surface gives a positive (downward) normal force increment, with a peak corresponding closely to the attachment angle α_R in Fig. 8. (The exception is the relatively narrow NACA 0012 aerofoil, where the upper surface suction dominates and the increment is negative). For aspect ratios greater than critical, the separated flow increment falls to zero at around 45-60°. At very high incidences the base pressure depends on the wake flow structure, which in turn depends in a rather unpredictable way on the aspect ratio *L/D*.

The pitching moment characteristics are a little more complex, since these combine contributions from both the upper/lower surface and front/rear face pairs. Figure 10 indicates that the basic 'attached flow' contribution from one pair of faces follows a Sin2α-like curve (with possibly a small skew to the right). From purely geometric considerations, assuming similar aerodynamic behaviour on each face, the moment contribution from the short side will be of opposite sign to that from the long side, and smaller by a factor of $1/(L/D)^2$.

The combined 'attached flow' moment contributions (Fig. 12(b)) can then be represented by an equation of the form;

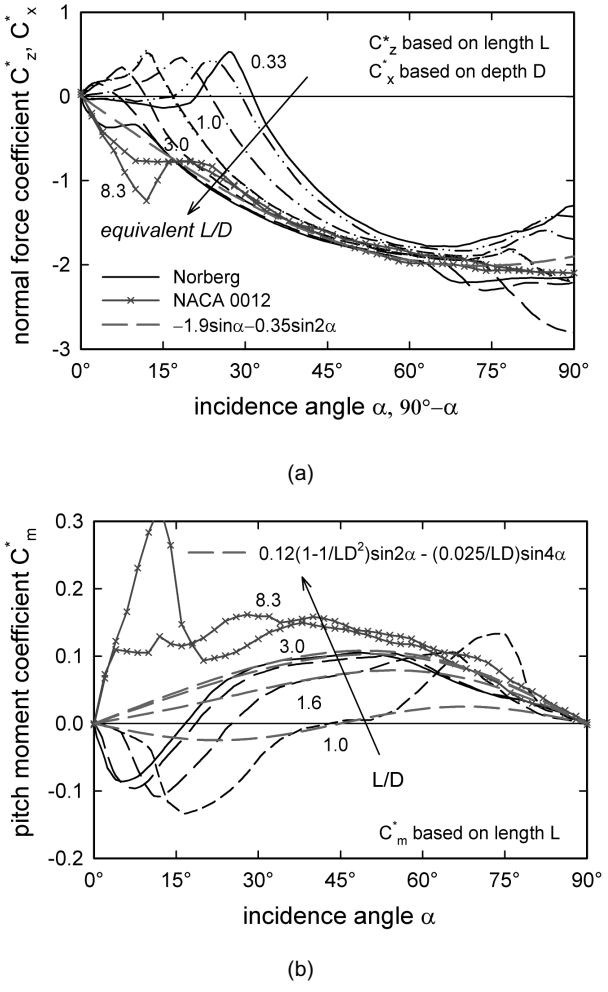

Figure 12. Effect of L/D on body axis force and moment for 2D prisms (with coefficients based on the corresponding side length).

$$C^*_m \approx 0{\cdot}12\left(1-\left(\frac{D}{L}\right)^2\right)\mathrm{Sin}2\alpha - 0{\cdot}025\left(\frac{D}{L}\right)\mathrm{Sin}4\alpha \qquad \ldots (2)$$

where the moment reference length is the length *L*. The Sin2α term is the sum of the opposing moment contributions from the front/rear and upper/lower faces. The additional Sin4α term corresponds to the small asymmetry seen in Fig. 10, and is presumably the result of an interaction between flows on adjacent faces.

For a square prism, the 'attached flow' component (dashed line in Fig. 12(b)) can be seen to be stabilising at 0° and 90° incidence, and destabilising at 45°. For the other prisms, this component is destabilising at low incidence (short side facing into the flow), but stabilising at high incidence (long side facing into the flow). The 'separated flow' contribution is always stabilising, with a peak increment corresponding closely again to the attachment angle α_R in Fig. 8.

3.0 3D AERODYNAMICS OF RECTANGULAR CONTAINERS

In contrast to the 2D case, there is relatively little experimental data available for 3D rectangular loads. There is also a significant level of variation between datasets, due perhaps to the highly unsteady nature of the flow and to the high levels of support interference found with conventional strut mounting.

https://doi.org/10.1017/S0001924000005650 Published online by Cambridge University Press

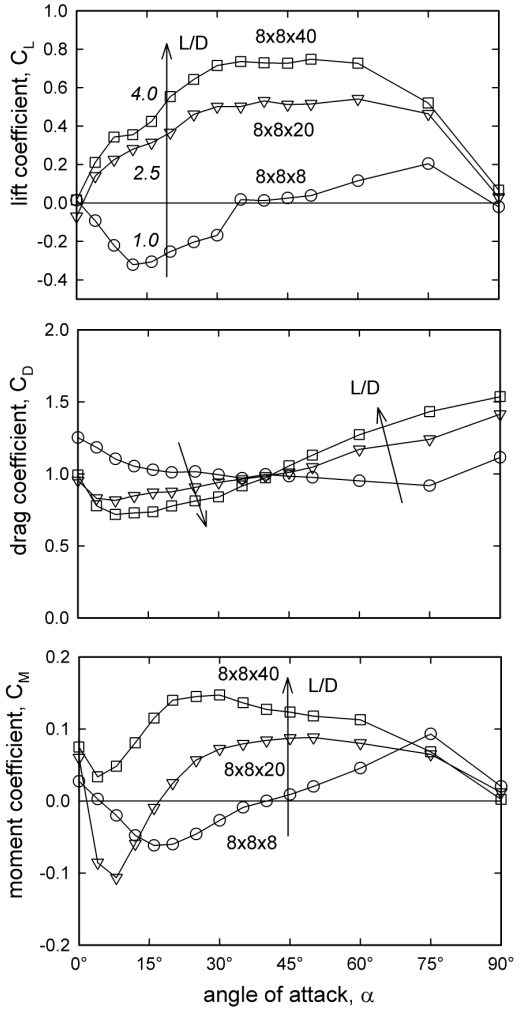

Figure 13. Lift, drag and pitching moment for three rectangular containers (data from[29], coefficients based of projected frontal area as Fig. 4).

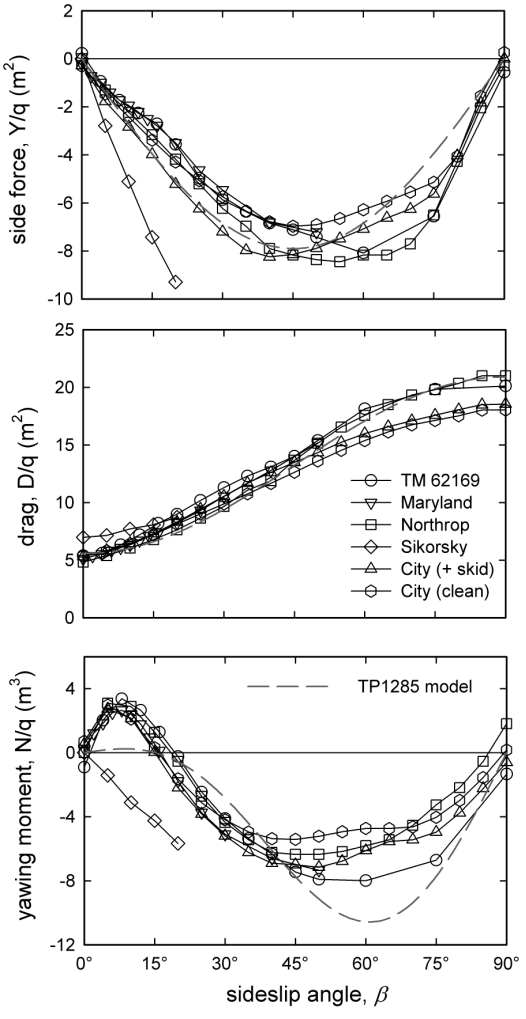

Figure 14. Comparison of MILVAN (8ft × 8ft × 20ft) aero datasets for planar yawing motion at zero angle of attack[9,26,27,28].

The majority of published data relates to the 8ft × 8ft × 20ft MILVAN container[11,15,26,27,28,29], with a review in Ref. 9), although some more work has been done recently on the 6ft × 6ft × 8ft CONEX container[30,31]. Only two sources provide any information on effect of shape, Ref. 29 from NASA (a data report which forms the basis of almost every MILVAN simulation model), and a rather little-known linked set of reports from the Royal Military College of Science (RMCS)[32,33,34].

3.1 'Planar' motion (pure α or β)

The basic planar (pure pitch or yaw) aerodynamic characteristics of 3D rectangular boxes are very similar to those of 2D prisms.

For example, Fig. 13 shows wind tunnel test data from NASA[29] for three standard boxes – an 8ft cube, an 8ft × 8ft × 20ft MILVAN container, and an 8ft × 8ft × 40ft shipping container. The data shown here is for smooth-sided, sharp-edged models, and since the boxes have a square front face, the pitch and yaw aerodynamics are essentially identical. (NB Ref. 29 also presents data for models with more representative corrugated surfaces, which rather surprisingly show very similar behaviour). The data has initially been non-dimensionalised using projected frontal area and height, simply in order to give a direct comparison with the 2D data shown in Fig. 4[18].

The variations in lift, drag and pitching moment with (*i*) incidence, and (*ii*) aspect ratio *L/D* are remarkably similar to the 2D case. However, overall magnitudes have reduced, and the 'separated flow' contributions at low incidences are much less pronounced. Nevertheless, it is clear from a comparison of Figs 3 and 13 that the basic box aerodynamics in 2D and 3D flows are very similar.

Looking specifically at the MILVAN container, Fig. 14 compares published data for wind-axis drag, sideforce and yawing moment variation with sideslip angle[9,26,27,28], for models with representative geometry (i.e. surface corrugations, base skids etc). Since underslung loads oscillate primarily in yaw, available datasets focus on providing a wide (±180°) sideslip angle range, with often a rather limited (±20-40°) angle-of-attack range.

MILVAN data is invariably given in wind axes, and usually in terms of forces and moments divided by dynamic pressure (giving units of m^2 and m^3 respectively). Many datasets define incidence in terms of Euler angles yaw ψ and pitch θ relative to the wind tunnel freestream direction. For this specific case only $\theta \equiv \alpha$ and $\psi \equiv -\beta$, so in order to avoid any possible confusion published data presented here will all be converted to aerodynamic incidence angles.

Two datasets show some variation from the general trend, indicating the significance of support interference in bluff body testing. Early Sikorsky data[27] shows a much higher sideforce at lower incidences, and an unstable yawing moment characteristic. Unpublished data from City University shows a 13% reduction in drag (and a smaller reduction in yawing moment) at higher incidences. The Sikorsky data is typical of excessive interference

https://doi.org/10.1017/S0001924000005650 Published online by Cambridge University Press

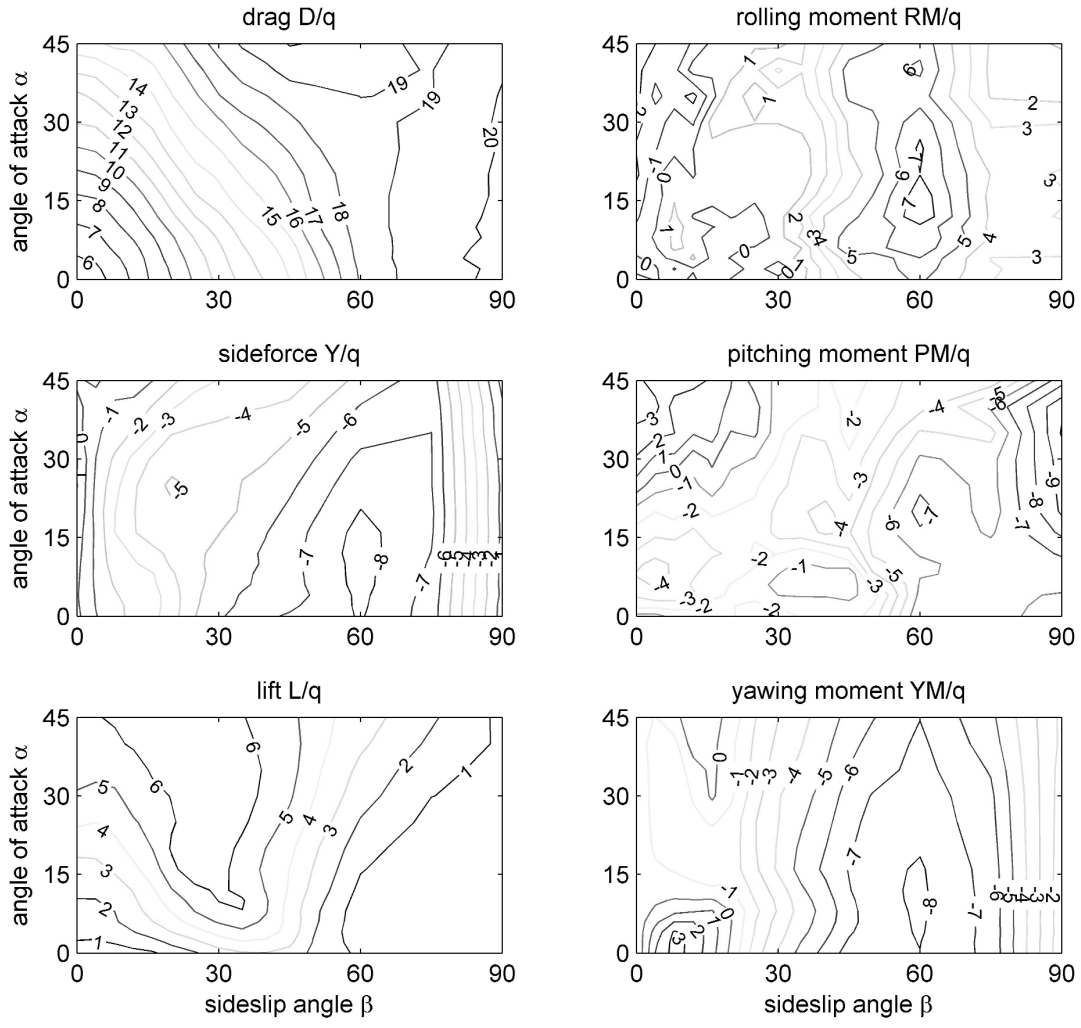

Figure 15. MILVAN forces and moments for non-planar (pitch + yaw) motion (wind axes, data from Ref 9, units m^2 for forces, m^3 for moments)

from too short a support strut (a similar result is reported in Ref. 11), while the tests at City used a multiple-point mounting more representative of a typical load sling. Reference 9 also notes that support tares for a strut mounted MILVAN model[29] determined in the usual manner using a dummy strut often appeared to be random.

3.2 Non-planar motion (coupled α and β)

3.2.1 Conventional representation

Having measured these aerodynamic characteristics, the next question is how to represent them within a flight dynamics model. One possibility is to use a large look-up table, but until recently many studies have used curve-fits to the data. Equation (3) shows a typical example, from a simulation model in Ref. 13. This trigonometric fit to the large-amplitude forces and moments (with a typo in the drag equation corrected), is shown as the dashed line on Fig. 14.

$$\begin{aligned}\frac{D}{q} &= 20\cdot 9 - 7\cdot 66\left(1+\mathrm{Cos}2\alpha\mathrm{Cos}2\beta\right)\\ \frac{Y}{q} &= -7\cdot 9\mathrm{Sin}2\beta\mathrm{Cos}2\alpha \qquad \ldots (3)\\ \frac{N}{q} &= -7\cdot 73\mathrm{Sin}2\beta + 4\cdot 47\mathrm{Sin}4\beta\left|\mathrm{Cos}\alpha\right|\end{aligned}$$

This type of curve-fit does a reasonable job for sideforce and drag, but clearly struggles with the more complex yawing moment characteristics.

The reasons for this can be seen if a 'full' dataset is examined. Fig. 15 shows wind-axis forces and moments for a MILVAN model, replotted from tabulated data in Ref. 9, which in turn was derived from a careful re-analysis of data from Ref. 29. Note that this data is in dimensional form, ie 'parasite drag area' and 'moment volume'.

The complexity of the data is immediately apparent, and Ref. 9 devotes considerable effort to identifying symmetry properties in an attempt to (a) simplify the data representation, and (b) to provide a rational means of correcting for experimental errors and extrapolating to higher pitch angles. The data itself is simply presented as a set of six 2D look-up tables – ie forces and moments as functions of pitch and yaw angle.

3.2.2 Body-axis forces

The problem with look-up tables or trigonometric curve-fits to data as complex as that shown in Fig. 15, is that neither gives any clue to the underlying flow physics. As a result, any change to container geometry requires the model to be regenerated from scratch – a lengthy and costly process, and hence seldom done.

Such a reliance on empirical modelling should have been a cause for concern before now; but nowhere in the literature has the basic form of the container aerodynamic model ever been questioned.

https://doi.org/10.1017/S0001924000005650 Published online by Cambridge University Press

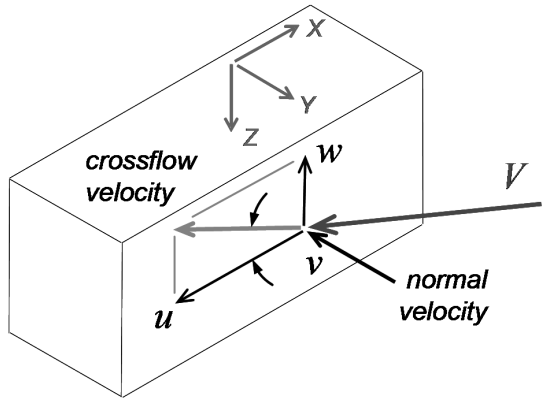

Figure 16. Incidence parameters *v/V* and $\tan^{-1}(w/u)$ for side-face forces and moments.

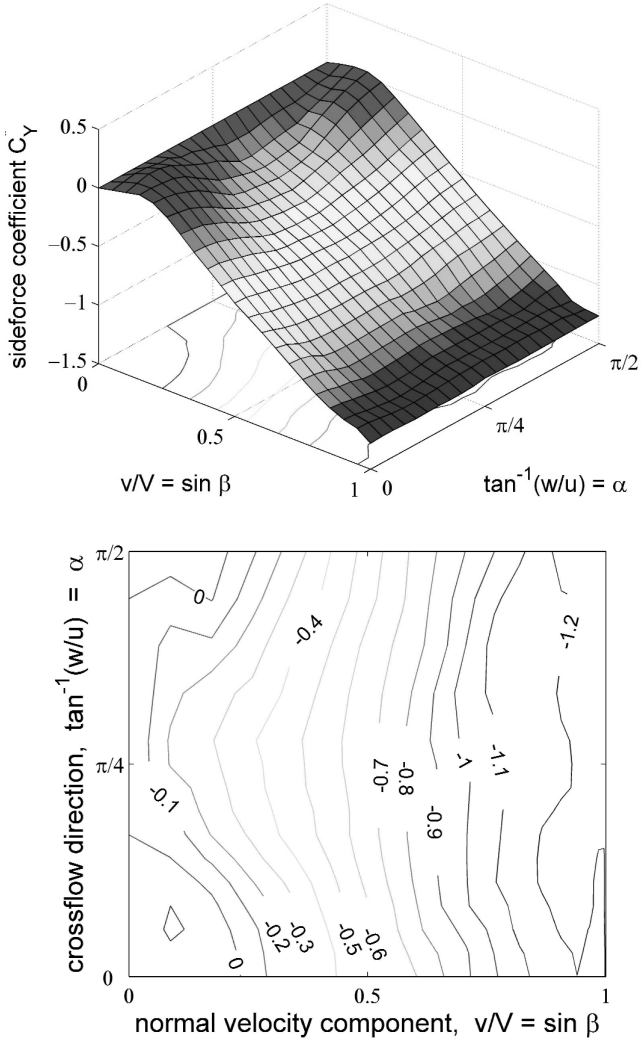

Figure 17. Variation of body axis sideforce coefficient C_Y^* with normal velocity and crossflow direction for a cube (data from[31]).

However, the discussion in Section 2.4 above (and a moment's consideration of the nature of the flow around a box), make it clear that body-axis rather than wind-axis forces are the appropriate variables.

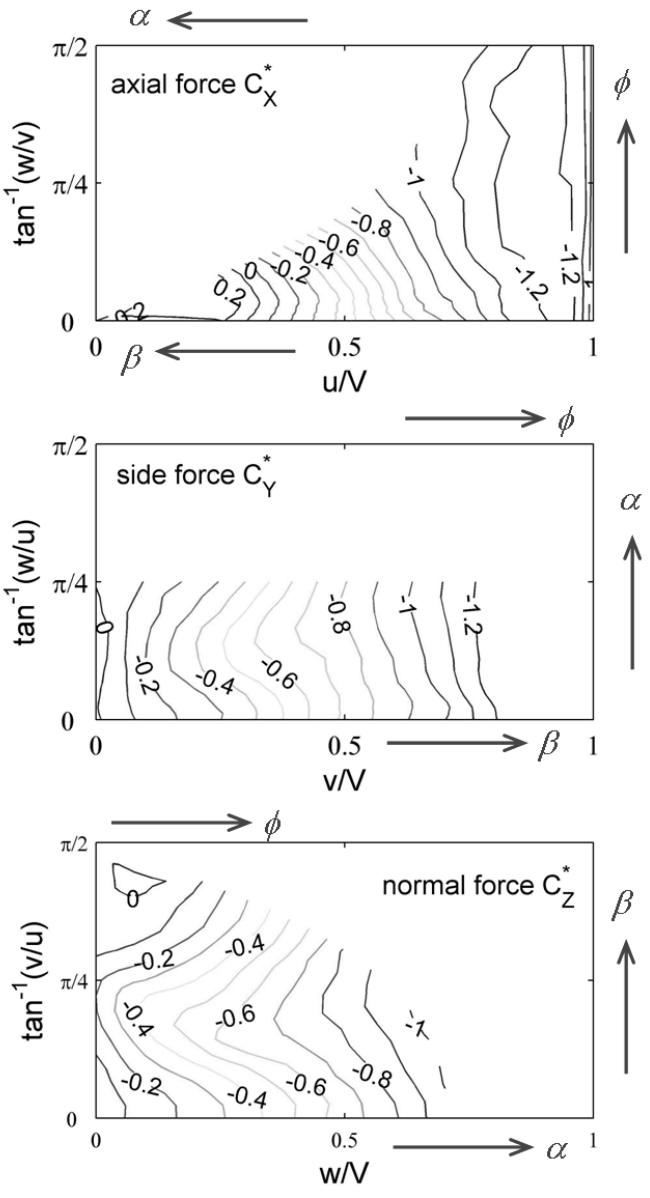

Figure 18. Variation of body axis force coefficients with normal velocity and cross-flow direction for a MILVAN container (data from [9]).

Further, what about the aerodynamic parameters, the conventional angle-of-attack α and sideslip angle β ? These are just one of many possible pairs of incidence angles, and are entirely appropriate for attached flow aerodynamics, but not necessarily for 2D bluff body flows.

Figure 12(a) gives an indication of a more appropriate definition:

1. the normal force on a given pair of faces is dependent on the angle of the flow relative to those faces,
2. when non-dimensionalised by the corresponding face area, the body-axis coefficients collapse onto a single basic curve, and
3. this basic variation is roughly sinusoidal.

The basic force curves in Fig. 12(a) then become

$$C_z^* \propto \mathrm{Sin}\alpha \propto \frac{w}{V}$$
$$C_x^* \propto \mathrm{Sin}(90° - \alpha) \propto \frac{u}{V} \quad \ldots (4)$$

https://doi.org/10.1017/S0001924000005650 Published online by Cambridge University Press

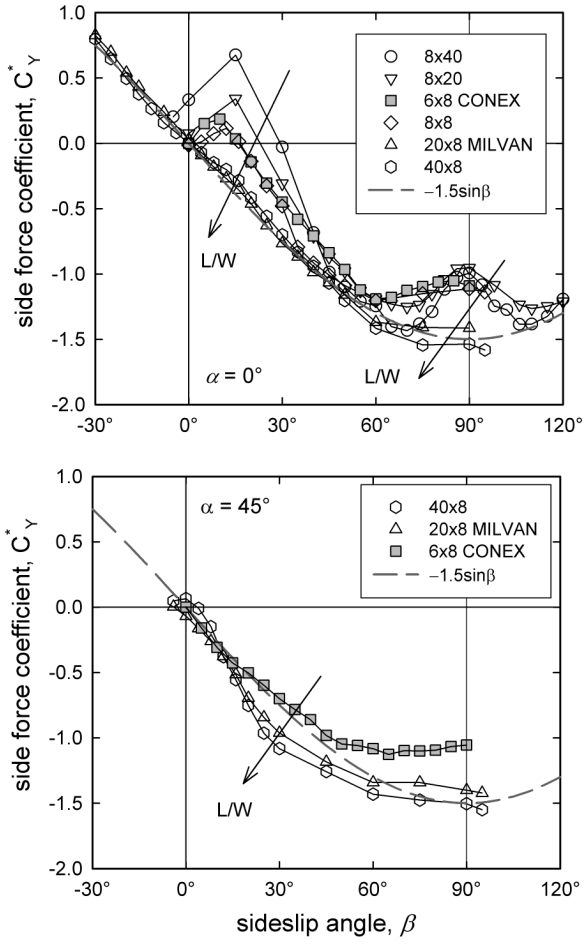

Figure 19. Effect of *L/W* on 3D body axis force scaling (data from[29,31]).

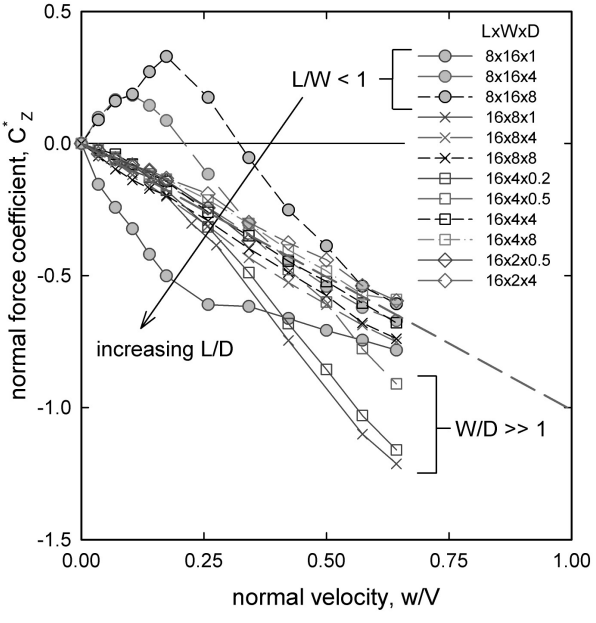

Figure 20. Effect of *L/W* and *W/D* on 3D body axis force scaling (data from[34])

since $\beta = 0$. In other words, the appropriate basic aerodynamic parameters for a rectangular box are the relative velocity components perpendicular to each pair of faces. The corresponding incidence parameter for the sideforce C_Y* would then be v/V. The reference areas for C_X^*, C_Y^* and C_Z^* are the areas of the front, side and top faces of the box respectively.

For non-planar flow a second incidence parameter is required. In order to complete the (u,v,w) triple, an obvious choice is the direction of the cross-flow velocity component parallel to the face in question (Fig. 16), since this will govern which edge the flow separates from. The new incidence parameters are then:

$$
\begin{aligned}
C_X^* &= fn\left(\frac{u}{V},\ \mathrm{Tan}^{-1}\frac{w}{v}\right) = fn\left(\frac{u}{V},\ \phi^*\right)\\
C_Y^* &= fn\left(\frac{v}{V},\ \mathrm{Tan}^{-1}\frac{w}{u}\right) = fn\left(\frac{v}{V},\ \theta^*\right) \equiv fn\left(\mathrm{Sin}\beta, \alpha\right)\\
C_Z^* &= fn\left(\frac{w}{V},\ \mathrm{Tan}^{-1}\frac{v}{u}\right) = fn\left(\frac{w}{V},\ \psi^*\right)
\end{aligned}
\qquad \ldots (5)
$$

For a rectangular box a complete aerodynamic model is obtained for $0 \le u/V,\ v/V,\ w/V \le +1$ and $0 \le \phi^*,\theta^*,\psi^* \le +\pi/2$. Forces and moments for incidence angles outside this range are readily obtained from symmetry principles[9].

To demonstrate the application of these parameters, Fig. 17 shows side-force coefficient C_Y^* (non-dimensionalised using the side face area) for a sharp-edged cube plotted against velocity component normal to the side face v/V and cross-flow velocity direction relative to the side face $\mathrm{Tan}^{-1}(w/u)$, Fig. 16. This data is taken from Ref. 31, which is unique in providing not only high quality data over the full (±90°, ±180°) pitch/yaw range, but also the results of an extensive study of support interference. Essentially the same results were obtained for C_X^* and C_Z^*. Symmetry considerations dictate that the 'normal' force is zero at the left-hand edge and constant along the right-hand edge of Fig. 17(b), and that the plot is symmetric about $\mathrm{Tan}^{-1}(w/u) = 0$ and antisymmetric about $v/V = 0$.

Immediately, a significant improvement in the data presentation is evident. The overall trend with v/V is almost linear, with very little variation with crossflow direction above $v/V \sim 0{\cdot}5$. At lower values of v/V there are two symmetrically placed dips in sideforce, centred about cross-flow directions of zero (flow approaching directly from the front of the body) and $\pi/2$ (flow approaching directly from above or below the body). This is the separation bubble contribution discussed previously, which is now much easier to see. At an intermediate cross-flow direction of $\pi/4$ (45°) a closed separation bubble cannot form; instead side-edge vortices on the leeward face maintain essentially an attached flow.

The sharp-edged cube data indicates that this approach has the potential to greatly simplify the modelling of the force data, but as a symmetric object does not provide evidence for its general applicability.

In order to do so, Fig. 18 shows the MILVAN model force data from Fig. 15[9] re-plotted using Equation (5). The results are very encouraging, with the general form of Fig. 17 repeated for all three components, in both shape and magnitude. As one might expect, there is some asymmetry in the 'long' face forces (sideforce C_Y^* and normal force C_z^*), due to the 2.5:1 aspect ratio. The dip in the lower left corner in these two plots corresponds to a separation bubble forming from the forward (short) edge, and the dip in the upper left to a larger bubble forming from the side (long) edge.

Also indicated on Fig. 18 for ease of interpretation are the equivalent changes in conventional incidence angles α and β, and body-axis roll angle ϕ. For example, on the axial force plot, moving to the left along the lower edge corresponds to increasing sideslip angle, and to the left along the upper edge to increasing angle of attack. Moving upwards along the right-hand edge corresponds to increasing roll angle.

https://doi.org/10.1017/S0001924000005650 Published online by Cambridge University Press

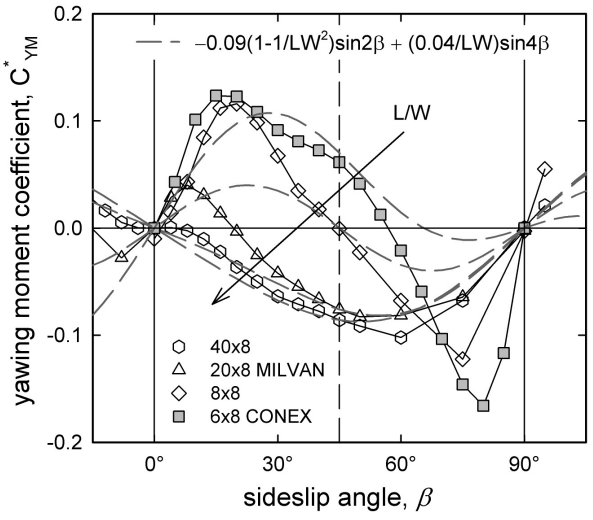

Figure 21. Effect of *L/W* on 3D moment scaling (yawing moment coefficients based on side face area and length) (data from Refs 29 and 31).

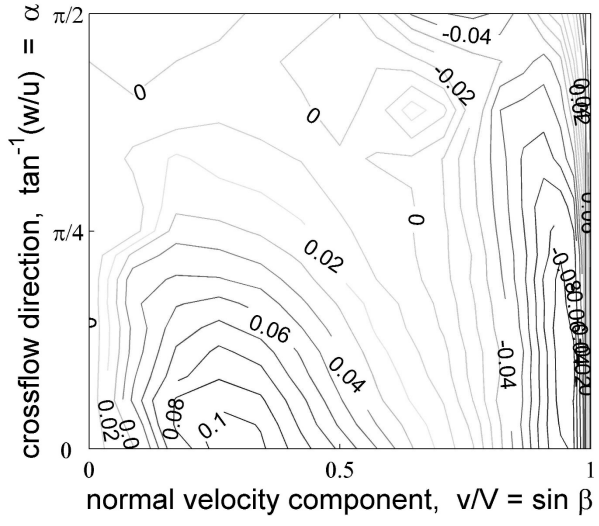

Figure 22. Variation of body axis yawing moment coefficient *C*YM* with normal velocity and crossflow direction for a cube[31].

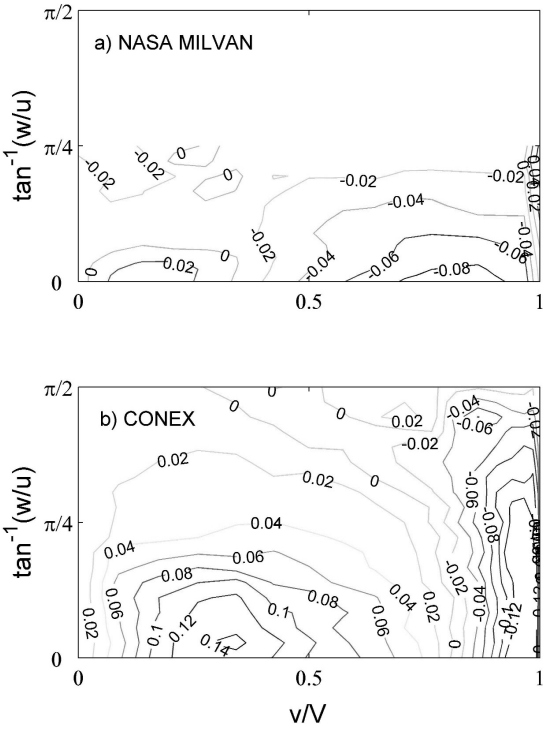

Figure 23. Variation of body axis yawing moment coefficient C*YM with normal velocity and crossflow direction for MILVAN and CONEX containers (data from[9,31]).

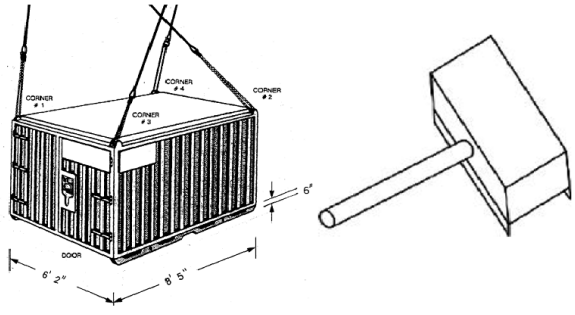

Figure 24. 8ft × 6ft × 6ft CONEX container, with model as tested in[31].

Visual assessments of contour plots are notoriously subjective, so Fig. 19 provides a direct comparison of the effect of sideslip angle β on sideforce coefficients for a number of strut-mounted box models[29,31], at angles of attack of 0° and 45°. The box geometries are now characterised by their length/width ratio *L/W* (the appropriate aspect ratio for lateral forces), with *W/D* = 1 in all cases. (NB the 8 × 40 and 8 × 20 boxes in Fig. 19 are simply the 40 × 8 and 20 × 8 boxes from Ref. 29 yawed by 90°).

The behaviour at 0° pitch is essentially identical to the 2D prism data in Fig. 12(a), with all curves converging to a limiting 'attached flow' sine curve

$$C_Y^* \approx -1{\cdot}5\mathrm{Sin}\beta = -1{\cdot}5\frac{v}{V} \qquad \ldots (6)$$

The 3D lift-curve-slope is reduced from –1·9 to –1·5 compared with 2D flow. As before, the magnitude of the separation bubble contribution reduces, and the peak point moves forward, as aspect ratio *L/W* increases (and α_R reduces). The 'base-dip' at high incidences shows a more consistent variation with aspect ratio than for the 2D case, becoming steadily larger as *L/W* reduces.

At 45° pitch angle the picture is a little less clear. The almost-cubical CONEX container follows the 'attached flow' sine curve, with a large base-dip very similar to the 0° pitch case. The longer boxes (*L/W* = 2·5 and 5·0) rise above this line before falling back to the same base pressure as at 0° – probably indicating the presence of some vortex lift from a side-edge vortex along the long edge (flow visualisation in[11]).

Further confirmation of the general nature of the normal velocity scaling is given by Fig. 20, which re-plots data from Ref. 34 for a wide range of higher aspect-ratio box shapes. This dataset from RMCS presents lift and drag variations with pitch angle (up to 40°), for models suspended in the wind-tunnel using a four-point wire mounting. When converted to body-axis form, the majority of the data collapses onto a linear variation with normal velocity component (*u/V* or *w/V*), with a slope of –1·0.

The reduction in slope compared with Fig. 20 is consistent with the effect of support system seen in Fig. 14, indicating that strut mounted model tests may over-predict container drag by 10-20%.

As in Fig. 19, only boxes with their long side facing the flow (ie

https://doi.org/10.1017/S0001924000005650 Published online by Cambridge University Press

$L/W < 1$) show any significant effect of separated flow at lower incidences. This goes from a positive increment for low L/D (lower surface bubble) to negative for high L/D (thin plate with aerofoil-like flow on upper surface). At intermediate incidences some of the flatter slender shapes (high W/D, high L/D) show signs of a non-linear vortex lift increment similar to that seen on slender wings. Also of note is that axial force data from Ref. 34 shows a much later (and smaller) base pressure dip at high incidence, again suggesting a significant effect of support interference.

3.2.3 Body-axis moments

The same approach can be applied to body axis moments, with Fig. 21 showing that 3D moment characteristics for a range of typical load geometries vary with incidence angle and aspect ratio in a very similar manner to the 2D data in Fig. 12(b). The basic 'attached flow' variation (dashed line) modelled by Equation (7) is identical in form to Equation (2), with L/W as the appropriate aspect ratio for yaw as opposed to pitch motion.

$$C^*_{YM} \approx -0{\cdot}09\left(1-\left(\frac{W}{L}\right)^2\right)\mathrm{Sin}2\beta + 0.04\left(\frac{W}{L}\right)\mathrm{Sin}4\beta \qquad \ldots (7)$$

The overall yawing moments are reduced compared to the 2D case, although the aspect ratio dependent asymmetry represented by the 2nd term has increased.

Using the cube data from Ref. 31 as a starting point, Fig. 22 shows the variation of body-axis yawing moment with side face normal velocity component v/V and cross-flow direction $\mathrm{Tan}^{-1}(w/u)$. Two large 'separated flow' peaks at low and high incidence are clearly evident, the left hand peak from the left/right pair of faces, and the right hand peak from the front/rear side pair of faces. A similar picture is obtained if the front face parameters u/V and $\mathrm{Tan}^{-1}(w/v)$ are used, but with the relative extents of the two peaks reversed.

Symmetry considerations constrain the moment to zero along the right, left and upper edges of the plot. The moment characteristics are symmetric about $\mathrm{Tan}^{-1}(w/u) = 0$, and antisymmetric about $v/V = 0$.

Plotting yawing moment data for the CONEX[31] and MILVAN[9] containers (Fig. 23) gives a very similar picture. For the CONEX container, essentially the same results are obtained for all three axes. For the MILVAN container the pitching moment data (plotted *vs* w/V and $\mathrm{Tan}^{-1}(v/u)$) is similar but less extensive, while the rolling moment data is unreliable (as noted in Ref. 9, possibly due to support interference effects from a large ventral strut mounting[29]).

4.0 3D MODELLING

In order to illustrate the application of the modelling approach described above, the lateral-directional aerodynamics (sideforce and yawing moment) of a CONEX container (Fig. 24) will be briefly analysed, using data from Ref. 31. The aerodynamic characteristics of this container are similar in form to the more common MILVAN (Figs 12 and 21), but with rather larger separated flow increments, giving a more severe test. The baseline orientation for this container is with the longer side facing into the flow (i.e. $L/W = 0{\cdot}75$, $L/D = 1{\cdot}0$).

4.1 Body-axis forces

Figure 24(a) shows the variation of the body-axis sideforce coefficient C_Y^* with the side face normal velocity component v/V and crossflow direction $\theta^* = \mathrm{Tan}^{-1}(w/u)$. The reference area used is the side face area (6ft × 6ft). The general behaviour is similar to that of the cube model shown in Fig. 16, albeit with more pronounced separation bubble increments at low incidences, and a clear dip in base pressure at high incidence (Fig. 18).

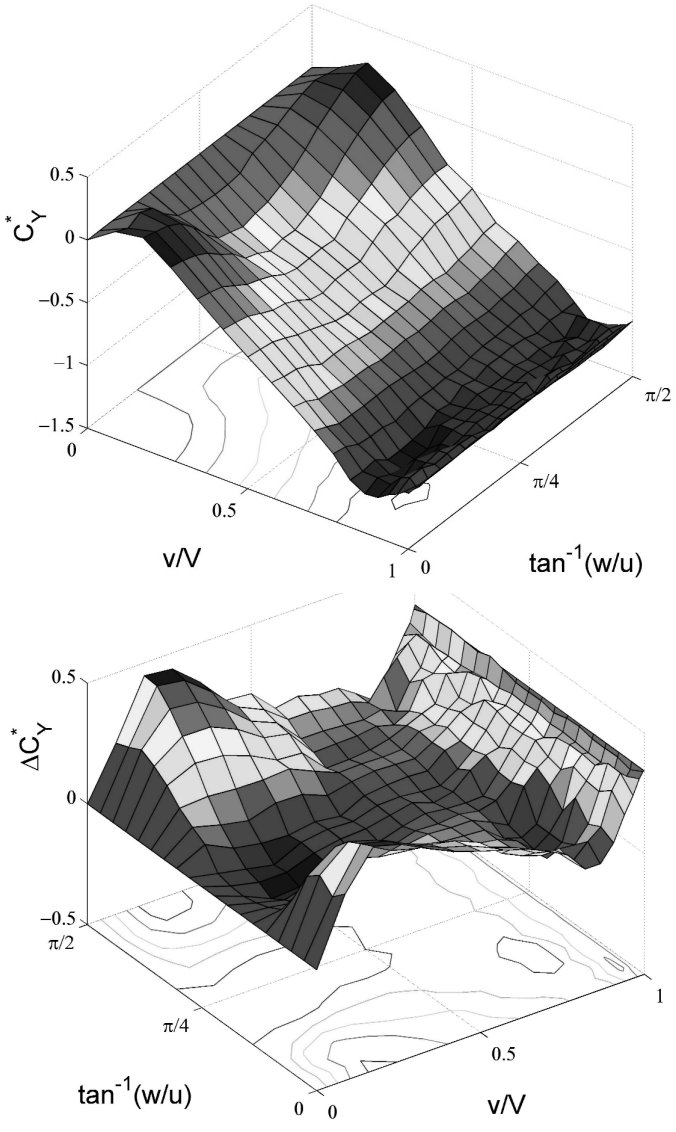

Figure 25. Effect of linear trend removal on CONEX body-axis side-force (data from Ref. 31).

The first step in modelling this response is to remove the basic 'attached flow' linear response,

$$C^*_{Y,att} \approx -1{\cdot}4\mathrm{Sin}\beta = -1{\cdot}4\frac{v}{V} \qquad \ldots (8)$$

to give the 'separated flow' component ΔC_Y^*. (There is a small reduction from the general trend of Fig. 18, probably due to a less intrusive strut geometry than in Ref. 29).

Having done so, Fig. 24(b) shows the separation bubble and base-dip sideforce increments much more clearly.

Modelling these separated flow contributions can be done in two further steps. Firstly, the increments at zero crossflow inclination (equivalent in this case to zero pitch angle) can be represented by two piecewise fits, Fig. 26. This shows the 'separated flow' mesh plot of Fig. 25 viewed from the side, to illustrate the general effect of normal velocity v/V. The base-dip (blue line) rises linearly from zero at $v/V \approx 0{\cdot}82$ (55° sideslip) to a maximum value of +0·35 with the flow perpendicular to the side face. The magnitude and onset of the base-dip is almost unaffected by crossflow direction. The separation bubble increment (dashed line) has a peak of +0·45 at $v/V \approx 0{\cdot}18$ (10° sideslip), but reduces rapidly to zero at a crossflow inclination of 45°.

https://doi.org/10.1017/S0001924000005650 Published online by Cambridge University Press

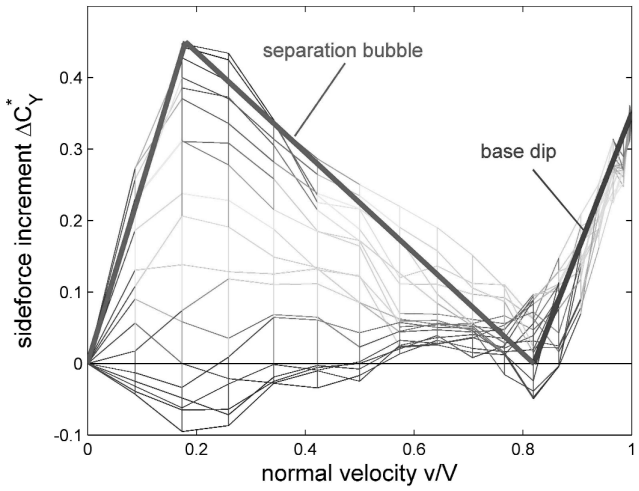

Figure 26. Piecewise linear fit to CONEX body-axis sideforce increment at zero pitch.

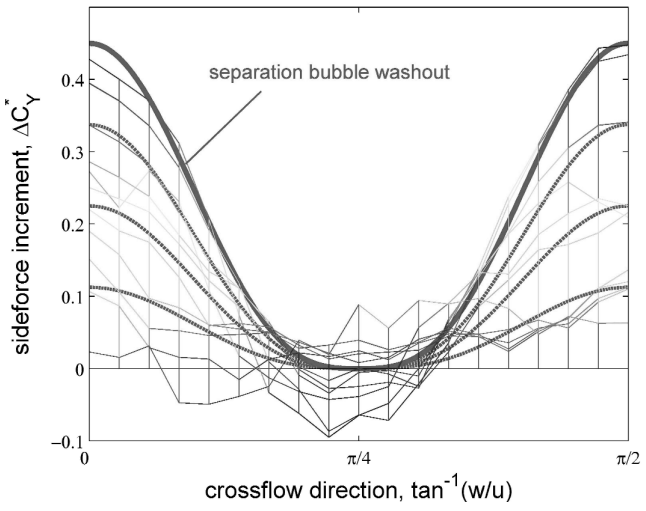

Figure 27. Separation bubble washout with pitch for CONEX body-axis sideforce increment.

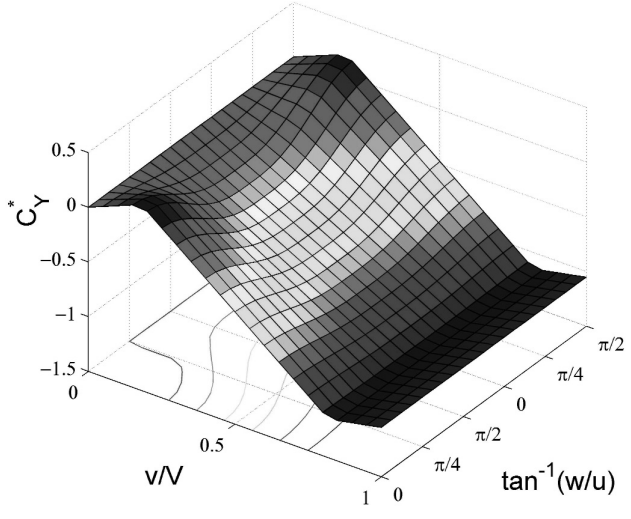

Figure 28. Basic 5-parameter fit to CONEX sideforce.

A more slender container (i.e. higher *L/W*) would have a smaller peak (Figs 12 and 19) at a lower incidence (lower α_R), but superimposed on the same 'attached flow' curve.

Secondly, having determined the separated flow increments at zero pitch/crossflow direction, it remains to model the variation with crossflow direction. The base-dip is essentially constant, but Fig. 25 shows a strong crossflow effect on the low incidence bubble increment. A number of different functions could be used to model this effect – for the purposes of this discussion, a simple trigonometric washout was used

$$\Delta C_Y^* = \Delta C_{Y,0}^* (v/V) \times \left| Cos^3 (2\theta^*) \right| \quad \ldots (9)$$

where θ^* is the crossflow angle $\mathrm{Tan}^{-1}(w/u)$. Figure 27 shows this washout model superimposed on the 'separated flow' mesh plot of Fig. 25, viewed from the front to show the general effect of crossflow direction.

Taking Equation (8), adding the piecewise linear separated flow fits of Fig. 26, and then reducing the bubble contribution using Equation (9) gives the modelled sideforce characteristics shown in Fig. 28.

The comparison with the experimental data of Fig. 25(a) is very good, yet this surface is defined by just five parameters:

1. the basic attached flow slope (–1·4 to –1·5 for 3D containers),
2. the base pressure dip – governed by the aspect ratio,
3. the magnitude of the separation bubble – governed by the aspect ratio,
4. the peak incidence (α_R) – governed by the aspect ratio, and
5. the break between separation bubble and base-dip (0·8 – 0·9 for 3D containers),

of which only 3. and 4. show a significant variation with box geometry.

4.2 Body-axis moments

A similar modelling approach can be applied to body-axis moments, although the structure is more complex because each moment has contributions from two pairs of faces.

Taking the CONEX yawing moment as an example, Fig. 29 shows the effect of yaw angle on yawing moment coefficient at zero pitch (with moments non-dimensionalised using the side face area and length).

The basic attached flow moment (dashed line) is modelled using the general form of Equation (7), with coefficients adjusted to match this specific case more closely.

$$C_{YM,0}^* = -0\cdot075\left(1-\left(\frac{W}{L}\right)^2\right)\mathrm{Sin}2\beta + 0\cdot03\left(\frac{W}{L}\right)\mathrm{Sin}4\beta \quad \ldots (10)$$

This can then be split into 'Sin2β' contributions from the two pairs of faces, plus a 'Sin4β' coupling term

$$\begin{aligned} C_{YM\,0,side}^* &= -0\cdot075\mathrm{Sin}2\beta \\ C_{YM\,0,front}^* &= +0\cdot075\left(\frac{W}{L}\right)^2\mathrm{Sin}2\beta \\ C_{YM\,0,side+front}^* &= +0\cdot03\left(\frac{W}{L}\right)\mathrm{Sin}4\beta \end{aligned} \quad \ldots (11)$$

However, unlike the normal force 'attached flow' these components cannot be independent of the crossflow direction, since the yawing moments must go to zero at three out of four edges in the (normal velocity, crossflow) domain.

The side face and coupling contributions are assumed to governed by the normal velocity component *v/V* (≡ Sinβ) and crossflow (pitch)

https://doi.org/10.1017/S0001924000005650 Published online by Cambridge University Press

direction $\theta^* = \mathrm{Tan}^{-1}(w/u)$. The front face contribution is governed by the normal velocity component u/V (≡ Cosβ at zero pitch) and crossflow (roll) direction $\phi^* = \mathrm{Tan}(w/v)$. The Sin2β and Sin4β terms in Equation (11) can readily be converted into functions of u/V and v/V as required using standard trigonometry formulae.

The variation with crossflow is rather less rapid than for the sideforce, and so a suitable washout function for a preliminary model is simply the cosine of the appropriate crossflow angle, so that;

$$C^*_{YM,side} = C^*_{YM,0}(v/V)\times\mathrm{Cos}(\theta^*)$$
$$C^*_{YM,front} = C^*_{YM,0}(u/V)\times\mathrm{Cos}(\phi^*) \quad \ldots (12)$$

Given that the largest contribution to yawing moment for this particular container comes from the front and rear faces, Fig. 30(a) plots the moment against the front face aerodynamic parameters u/V and $\mathrm{Tan}^{-1}(w/v)$. Subtracting the attached flow contribution of Equation (11) (washed out with crossflow angle using Equation (12) gives the nominal 'separated flow' component ΔC^*_{YM} in Fig. 30(b).

This component is close to zero over most of the range, with two main peaks corresponding to the separation bubble contributions on the front/rear and side faces. The right-hand (and smaller) is due to the separation bubbles on the side (shorter) faces. The left-hand larger increment is due to the bubbles on the front/rear (longer) faces. There is an additional small peak half way along the left-hand edge, which may be due to the formation of a side-edge vortex. A similar small peak is seen in the MILVAN data of Ref. 9, when plotted in the same way.

The two main separated flow contributions can be represented (as a first approximation) by piecewise linear fits, in a similar manner to the sideforce. Figure 31 shows the 'separated flow' yawing moment component from Fig. 30(b) plotted against both normal velocities (u/V and v/V).

The front face bubble increment depends on u/V, with a peak of –0·18 at $u/V \approx 0{\cdot}2$ (90–12° = 78° sideslip), falling to zero at 0·7 (45° sideslip). The side face bubble increment depends on v/V, with a peak of +0·07 at $v/V \approx 0{\cdot}28$ (16° sideslip), falling to zero at 0·6 (37° sideslip). Within the constraints of a simple linear fit, these values are consistent with the bubble reattachment angles of Fig. 8, and with complete flow reattachment at 45°.

Finally, the two bubble contributions need to be washed out with the appropriate crossflow angle – using $\mathrm{Cos}^2(\theta^*)$ and $\mathrm{Cos}^2(\phi^*)$ as a first approximation gives the modelled yawing moment characteristics shown in Fig. 32. Again, the comparison with the experimental data of Fig. 30(a) is excellent, with only three more parameters needed to define the fit:

1. the basic symmetric attached flow slope (0·075 to 0·09 for 3D containers),
2. the asymmetric attached flow slope (0·03 to 0·04 for 3D containers),
3. the magnitude of the front face separation bubble – governed by the aspect ratio
4. the peak incidence (α_R) for the front face bubble – governed by the aspect ratio,
5. the magnitude of the side face separation bubble – governed by the aspect ratio
6. the peak incidence (α_R) for the side face bubble – governed by the aspect ratio, and
7. the upper extent of the separation bubble components for front and side faces (0·6 – 0·7 for 3D containers)

of which only 3. to 6. above show a significant variation with box geometry. Having split out the side face separation bubble contributions to force and moments, the effects of increased turbulence and Reynolds Number (early reattachment) and corner rounding (delayed bubble formation) can readily be included

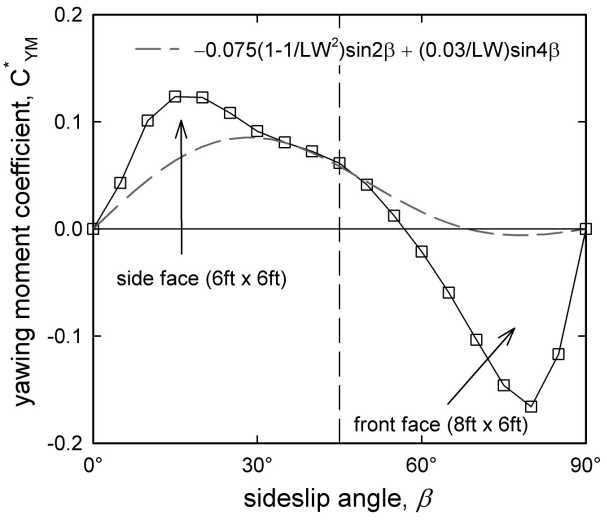

Figure 29. Attached and separated flow contributions to CONEX yawing moment (data from Ref. 31).

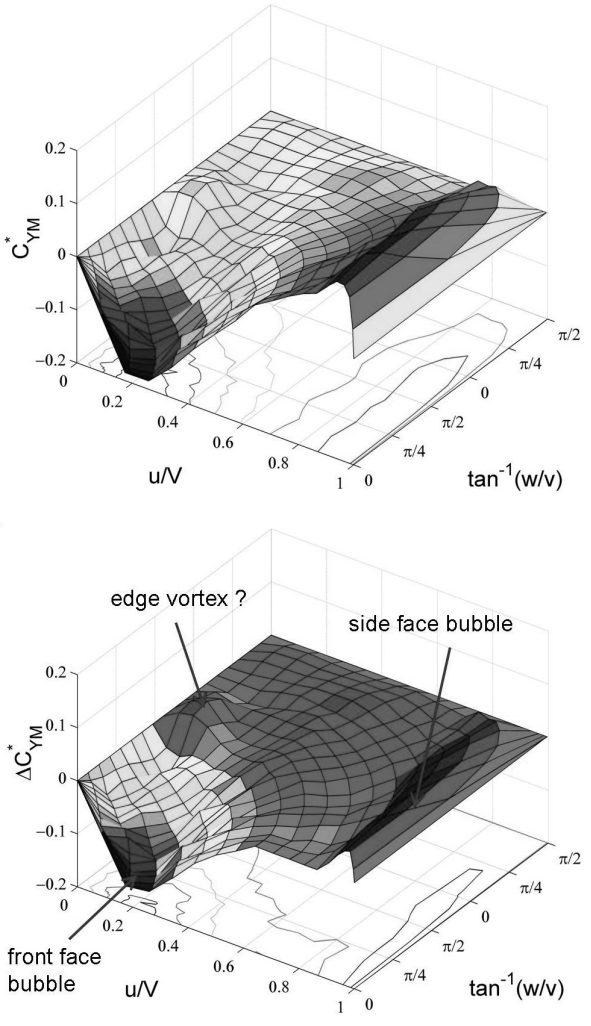

Figure 30. Effect of 'attached flow' removal on CONEX body-axis yawing moment.

https://doi.org/10.1017/S0001924000005650 Published online by Cambridge University Press

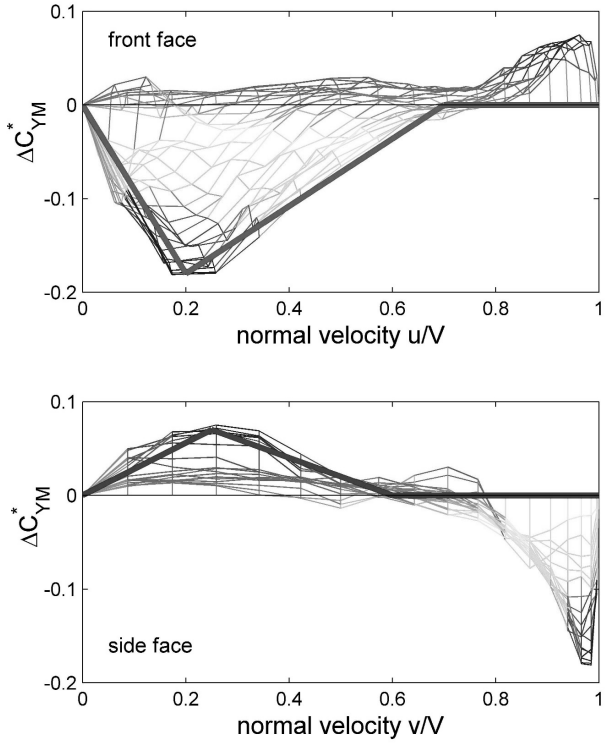

Figure 31. Piecewise linear fits to separated flow contributions to CONEX yawing moment.

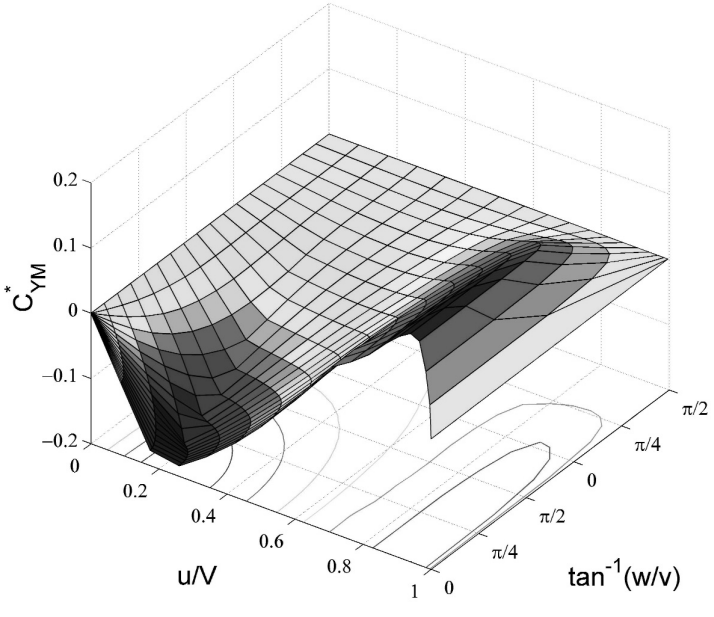

Figure 32. Basic 7-parameter fit to CONEX yawing moment.

5.0 CONCLUSIONS

A review of the aerodynamic characteristics of 2D and 3D rectangular boxes has shown that the basic forces and moments can be split into an 'attached flow' component and a 'separated flow' component. The first comprises the loads from the attached flow on the front face, the attached flow underlying the side face separation bubbles, and the fully separated base flow, and is independent of box geometry. The second component comprises the separated flow on the two side faces, which varies from full separation to a closed separation bubble depending on incidence and geometry.

Universal scaling rules have been determined. The 'attached flow' pressure distribution on a given face depends only on incidence, when the side face length L is used as a length scale. The 'separated flow' increment depends only on the underlying 'attached flow' pressure at the reattachment point. In turn, the bubble reattachment point depends only on incidence, when the adjacent front face length D is used as a length scale.

As a result, the aerodynamic characteristics of 2D and 3D boxes are found to be very similar, when non-dimensionalised correctly. Containers are rectangular bluff bodies, with the aerodynamic loads dominated by normal pressure forces. The loads therefore need to be considered in body axes, and not the universally used wind axes (which result in apparently highly complex variation in forces and moments with incidence). Further, the appropriate aerodynamic parameters are not the conventional angle of attack and sideslip angle, but the velocity components perpendicular to and parallel to each face.

The velocity component perpendicular to each face (u/V, v/V and w/V) governs the overall magnitude of the normal force and moments acting on that face, while the direction of the parallel (crossflow) velocity component governs which edge the flow separates from, and hence modifies the basic loading.

Recasting experimental data in this form, the aerodynamic characteristics of typical rectangular containers become much simpler in form, and more consistent in magnitude.

Body-axis forces are particularly straightforward. Each force component (axial, side, normal) is generated by the corresponding box face, with the basic attached flow component being directly proportional to the corresponding normal velocity component, so that for example $C^*_Y \propto v/V$. The 'lift-curve-slope' is essentially independent of aspect ratio, and ranges from –1·9 for 2D boxes to –1·5 for strut-mounted 3D box models to –1·2 for wire-mounted box models.

Superimposed on this basic force are small increments due to the separated flow. For normal velocities approaching 1 (ie flow perpendicular to the face), the wake flow structure appears to change, and the base pressure dips (becoming in general less negative). The magnitude of the base-dip depends on aspect ratio (reducing for more slender shapes, such as the MILVAN container), and appears to be significantly affected by support interference. At lower incidences the formation and disappearance of closed separation bubbles gives a more significant but also more localised increment, which depends on aspect ratio and on crossflow direction. For 0° and ±90° crossflow angle, the flow approaches an edge head-on and a closed separation bubble forms. For intermediate crossflow directions a closed bubble cannot form and the increment disappears – but a small side-edge vortex may form instead.

Body-axis moments are a little more complex, because each moment component is generated by two pairs of faces. Nevertheless, the basic moment contributions remain simple and consistent when analysed in terms of normal and crossflow velocities. Each pair generates opposing moments that vary with the sine of twice the local incidence angle, with the overall moment depending on the relative sizes of the faces. The magnitude of this moment contribution is almost independent of aspect ratio, ranging from +0·12 for 2D prisms to +0·09 for 3D boxes (depending on support interference levels). An additional asymmetric moment appears to be generated by a coupling between adjacent faces. The moment contribution from each face slowly reduces to zero as the crossflow angle increases from 0° to ±90°.

Superimposed on the basic moment curve are two separate increments from the two pairs of separation bubbles. The magnitude of these depend on the corresponding normal velocity component, and again both reduce to zero as the crossflow angle increases from 0° to ±90° (rather more rapidly than for the attached flow components).

https://doi.org/10.1017/S0001924000005650 Published online by Cambridge University Press

The universal nature of the 'attached flow' force and moment characteristics, coupled with 'separated flow' increments that can be adequately represented by piecewise-linear fits, means that modelling of the apparently complex aerodynamics of a container can be achieved with remarkably few parameters – of which only a small subset vary significantly with box geometry.

Further, this subset of parameters relates directly to the underlying flow physics. The magnitude and extent of the separated flow increments are directly governed by the magnitude and extent of the corresponding separation bubbles, which in turn depend on:

- incidence,
- box aspect ratio,
- corner radius,
- freestream turbulence level,
- Reynolds Number,
- wind tunnel support interference, and
- dynamic motion (pitch, yaw and roll rate)

The static modelling technique described here is therefore not just a modelling technique for flight dynamics simulations, but a prediction and analysis tool.

The universal scaling laws within the model structure (with a small number of empirical parameters derived from existing data) enable the a priori prediction of the aerodynamic characteristics of any new rectangular box load, and of the effects of geometry changes for an existing container. Extrapolation of existing data to incidence angles outside the original database becomes much more straightforward.

The relationship between bubble size and aerodynamic characteristics clarified by the model structure also provides a rational basis for correction/extrapolation of experimental data for turbulence, Re and tunnel interference effects.

Finally, the split into attached and separated load components gives a physical basis for the modelling of dynamic aerodynamic characteristics – for example the complex effects of motion frequency on the yaw damping derivative, for a MILVAN model reported in Ref. 11. A split into quasi-steady 'attached flow' and time-lagged 'separated flow' components has been very successful in the modelling of high-incidence aerodynamics of combat aircraft[35], and recent work at City suggests that similar success may be obtained for container dynamics.

REFERENCES

1. MATHESON, N. The stability of portable bridges carried on slings beneath helicopters, aerodynamics Report 154, DSTO, January 1980.
2. SHELDON, D.F. and PRYOR, J. Study in depth of a single point and two point lateral and tandem suspension of rectangular box loads, Technical Note AM/38, Royal Military College of Science, 1973.
3. STUCKEY, R.A. Mathematical modelling of helicopter slung-load systems, DSTO–TR–1257, December 2001.
4. CICOLANI, L.S. and EHLERS, G.E. Modelling and simulation of a helicopter slung load stabilization device, American Helicopter Society 58th Annual Forum, Montreal, Canada, June 2002.
5. PAVEL, M.D. Mathematical modelling of tandem helicopters with external sling loads for piloted simulations, AIAA-2006-6617, AIAA Modelling & Simulation Technologies Conference, Hilton Head, August 2007.
6. KENDRICK, S. and WALKER, D.J. The modelling, simulation and control of helicopters operating with external loads, 62nd American Helicopter Society Annual Forum, Phoenix, US, May 2006.
7. BISGAARD, M., BENDTSEN, J.D. and LA COUR-HARBO, A. Modeling of generic slung load system, *J Guidance, Control, and Dynamics*, March–April 2009, **32**, (2), pp 573-585.
8. DUQUE, E.P.N. *ET AL*, Reynolds-averaged Navier-Stokes simulations of helicopter slung loads, AHS International 4th Decennial Specialists' Conference on Aeromechanics, San Francisco, USA, January 2004.
9. CICOLANI, L. and KANNING, G. A comprehensive estimate of the static aerodynamic forces and moments of the 8- by 8- by 20-Foot Cargo Container, NASA TM 89433, May 1987.
10. ESDU, Fluid forces, pressures and moments on rectangular blocks, ESDU datasheet 71016, November 1978.
11. SIMPSON, A. and FLOWER, J.W. Unsteady aerodynamics of oscillating containers and application to the problem of dynamic stability of helicopter underslung loads, paper 13 in AGARD CP-235 Dynamic Stability Parameters, November 1978.
12. POLI, C. and CROMACK, D. Dynamics of slung bodies using a single-point suspension system, *J Aircr*, February 1973, **10**, (2), pp 80-86.
13. SHAUGHNESSY, J.D., DEAUX, T.N. and YENNI, K.R. Development and validation of a piloted simulation of a helicopter and external slung load, NASA TP-1285, January 1979.
14. WEBER, J.M., LIU, T.Y. and CHUNG, W. A Mathematical simulation model of the CH-47B helicopter, NASA TM-84351, August 1984
15. FEASTER, L., POLI, C. and KIRCHOFF, R. Dynamics of a slung load, *J Aircr*, February 1977, **14**, (2), pp 115-121.
16. RONEN, T. Dynamics of a Helicopter with a Sling Load, PhD. Thesis, Dept. of Aeronautics and Astronautics, Stanford University, USA, August 1985 (also AIAA-86-2288).
17. CICOLANI, L.S., DA SILVA, J.G.A., DUQUE, E.P.N. and TISCHLER, M.B. Unsteady aerodynamic model of a cargo container for slung-load simulation, *Aeronaut J*, July 2004, **108**, (1085), pp 357-368.
18. NORBERG, C. Flow around rectangular cylinders: pressure forces and wake frequencies, *J Wind Engineering and Industrial Aerodynamics*, 1993, **49**, pp 187-196.
19. MATSUMOTO, M. *et al*, Aerodynamic effects of the angle-of-attack on a rectangular prism, *J Wind Engineering and Industrial Aerodynamics*, **77** and **78**, 1998, pp 531-542.
20. LANEVILLE, A. and LU, Z.Y. Mean flow patterns around two-dimensional rectangular cylinders and their Interpretation, *J Wind Engineering and Industrial Aerodynamics*, 1983, **14**, pp 387-398.
21. LANEVILLE, A., GARTSHORE, I.S. and PARKINSON, G.V. An explanation of some effects of turbulence on bluff bodies', 4th International Conference on Wind Effects on Buildings and Structures, London, UK, September 1975.
22. ROBERTSON, J.M. *ET AL*, Wall pressures of separation-reattachment Flow on a square prism in uniform flow, *J Industrial Aerodynamics*, **2**, 1977/78, pp 345-359.
23. SANT'ANNA, F.A.D-M., LANEVILLE, A., TREPANIER, J.Y. and LU, Z.Y. Detailed pressure field measurements for some 2-D rectangular cylinders, *J Wind Engineering and Industrial Aerodynamics*, 1988, **28**, pp 241-250.
24. MULHEARN, P.J. Stagnation and reattachment lines on cylinder of square cross-section in smooth and turbulent flows, *Nature Physical Science*, **241**, 26th February 1973, pp 165-167.
25. LEISHMAN, J.G. *Principles of Helicopter Aerodynamics*, 2nd ed, Cambridge University Press, 2006.
26. WINDSOR, R.I. Wind tunnel tests of two models of rectangular containers, Wind Tunnel Report No 573. University of Maryland, Glenn L Martin Wind Tunnel, College Park, Maryland, USA, January 1970.
27. BRICZINSKI, S.J. and KARAS, G.R. Criteria for externally suspended helicopter loads, USAAMRDL TR-71-61, November 1971.
28. WATKINS, T.C., SINACORI, J.B. and KESLER, D.F. Stabilization of externally slung helicopter loads, USAAMRDL TR-74-42, August 1974.
29. LAUB, G.H. and KODANI, H.M. Wind tunnel investigation of aerodynamic characteristics of scale models of three rectangular shaped cargo containers, NASA TM-X 62169, July 1972.
30. CICOLANI, L.S., DA SILVA, J.G.A., DUQUE, E.P.N. and TISCHLER, M.B. Unsteady aerodynamic model of a cargo container for slung-load simulation, *Aeronaut J*, July 2004, **108**, (1085).
31. ROSEN, A., CECUTTAM S. and YAFFE, R., Wind tunnel tests of cube and CONEX Models, Technion report TAE-844, November 1999.
32. SHELDON, D.F. and PRYOR, J. Study in depth of a single point and two point lateral and tandem suspension of rectangular box loads, Technical Note AM/38, Royal Military College of Science, May 1973.
33. SHELDON, D.F. and PRYOR, J. A study on the stability and aerodynamic characteristics of particular military loads underslung from a Helicopter, Technical Note AM/40, Royal Military College of Science, April 1973.
34. SHELDON, D.F. and PRYOR, J. The aerodynamic characteristics of various rectangular box and closed cylinder loads, Technical Note AM/41, Royal Military College of Science, April 1973.
35. GREENWELL, D.I. A review of unsteady aerodynamic modelling for flight dynamics of manoeuvrable aircraft, AIAA-04-5276, AIAA Atmospheric Flight Mechanics Conference, August 2004.

https://doi.org/10.1017/S0001924000005650 Published online by Cambridge University Press

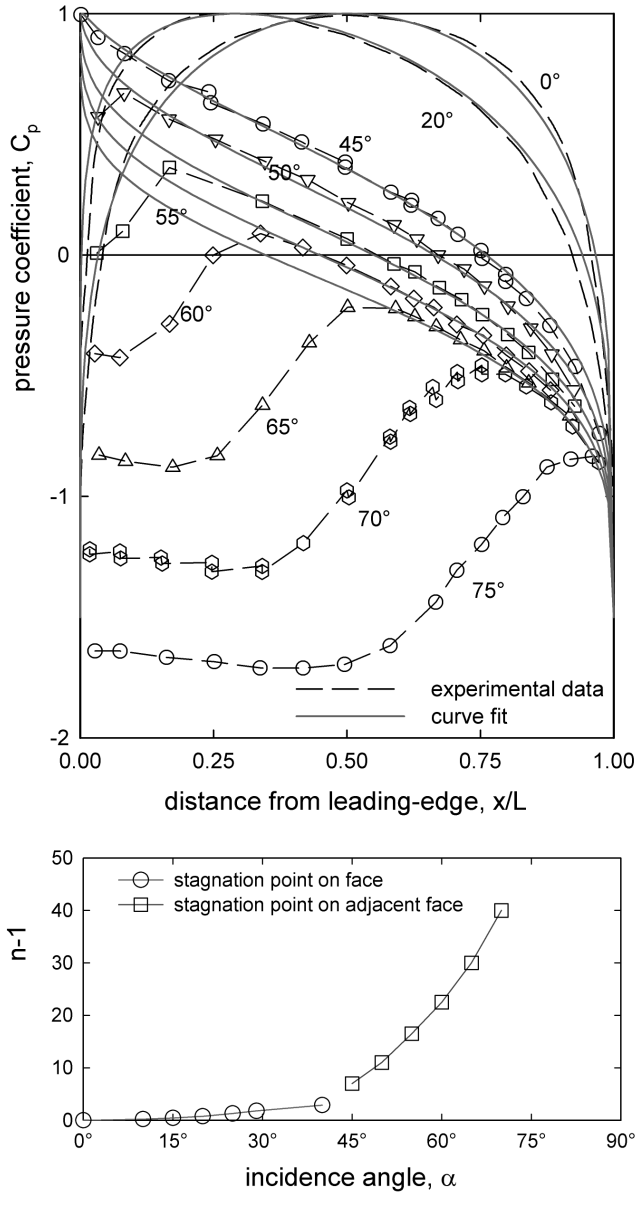

Figure A1. Fit to 'attached' flow component on 'front' face (data from Ref. (22)).

Appendix A Pressure Distribution on a 2D Rectangular Prism

An empirical fit to the underlying attached flow pressure distribution for both the front and side faces of a 2D rectangular prism, for pitch angles from 0° to 90° is

$$C_p = p(1 - C_{pB}) + C_{pB} \quad \ldots \text{(A1(a))}$$

where the basic pressure distribution shape is given by

$$p = (1 - w^2)^{1/4} \quad \ldots \text{(A1(b))}$$

and the asymmetry by

$$w = 2(x/L)^{1/n} - 1 \quad \ldots \text{(A1(c))}$$

where n is a function of incidence.

Appendix B CONEX Aerodynamic Model

This appendix gives an example of an implementation of the 3D model for the CONEX container (W = 8ft, L = 6ft[31]), for body-axis sideforce and yawing moment for normal velocities in the range 0+1 and crossflow angles in the range 0+π/2.

B1 3D Force Model

Aerodynamic forces are represented as body-axis forces, non-dimensionalised by the appropriate face area – ie side face area Ay for sideforce coefficient CY*. Each force is split into an 'attached' flow contribution which is a function of the appropriate normal velocity component, and a 'separated' flow contribution which is a function of normal velocity and cross-flow direction (Equation (B1)). So for example

$$C_Y^* = \frac{Y}{\frac{1}{2}\rho V^2 A_y} = C_{Y,att}^* + \Delta C_Y^* = -1{\cdot}4\frac{v}{V} + \left(C_{Y,bubble}^* + C_{Y,base\ dip}^*\right) \quad \ldots \text{(B1)}$$

Both separated flow components can be represented approximately as piecewise-linear functions of normal velocity (Fig. 26). The 'base dip' component (Equation (B2)) is independent of crossflow direction, while the 'separation bubble' component needs to be washed out with as cross flow angle changes (Fig. 27, Equation (9)).

$$C_{Y,base\ dip}^* = \begin{cases} 0; & v/V < 0{\cdot}82 \\ 1{\cdot}94\left(v/V - 0{\cdot}82\right); & v/V \geq 0{\cdot}82 \end{cases} \quad \ldots \text{(B2)}$$

$$C_{Y,bubble,0}^* = \begin{cases} 2{\cdot}5\,v/V\ ; & v/V \leq 0{\cdot}18 \\ 0{\cdot}45 - 0{\cdot}703\left(v/V - 0{\cdot}18\right)\ ; & 0{\cdot}18 < v/V < 0{\cdot}82 \\ \mathbf{0}\ ; & v/V \geq 0{\cdot}82 \end{cases} \quad \ldots \text{(B3)}$$

$$C_{Y,bubble}^* = C_{Y,bubble,0}^* \times \left|\mathrm{Cos}^3\left(2\theta^*\right)\right| \quad \ldots \text{(B4)}$$

As noted in Section 4.1, the sideforce model is defined by five parameters: the basic attached flow slope (= –1·4), the magnitude of the base pressure dip (= +0·35), the magnitude of the bubble component (= +0·45), the normal incidence at which this occurs (= 0·18), and the breakpoint between the bubble and base dip (= 0·82).

The axial force and normal force can be represented in a similar manner.

B2 3D Moment Model

Aerodynamic moments are represented as body-axis moments, non-dimensionalised by the appropriate face area and side length – ie side face area A_y and box length L for yawing moment coefficient C_{YM}^*

$$C_Y^* = \frac{YM}{\frac{1}{2}\rho V^2 A_y L} = C_{YM,att}^* + \Delta C_{YM}^* \quad \ldots \text{(B5)}$$

Aerodynamic moment modelling is rather more complex than for the forces because (a) body-axis moments have contributions from two pairs of faces, and (b) both attached and separated components are

https://doi.org/10.1017/S0001924000005650 Published online by Cambridge University Press

functions of crossflow direction.
In order to simplify the trigonometical expressions, we define two effective sideslip angles

$$\beta_{side} = \mathrm{Sin}^{-1}\left(\frac{v}{V}\right),\ \beta_{front} = \mathrm{Sin}^{-1}\left(\frac{u}{V}\right) \quad \ldots \text{(B6)}$$

Considering attached flow first, the moment model of Equation (11) (with the preliminary crossflow washout from Equation (12) becomes

$$C^{*}_{YM,att} = \left(-0{\cdot}075\,\mathrm{Sin}\,2\beta_{side} + 0{\cdot}03\left(\frac{8}{6}\right)\mathrm{Sin}\,4\beta_{side}\right)\mathrm{Cos}\left(\theta^{*}\right) + \left(0{\cdot}075\left(\frac{8}{6}\right)^{2}\mathrm{Sin}\,2\beta_{front}\right)\mathrm{Cos}\left(\phi^{*}\right) \quad \ldots \text{(B7)}$$

The separated flow moment components are represented by piecewise-linear functions (Fig. 31) of normal velocity washed out with crossflow angle.

$$C^{*}_{YM,bubble,side} = \begin{cases} +0{\cdot}25\,v/V\ ; & v/V \le 0{\cdot}28 \\ +0{\cdot}07 - 0{\cdot}219\left(v/V - 0{\cdot}28\right)\ ; & 0{\cdot}28 < v/V < 0{\cdot}6 \\ 0\ ; & v/V \ge 0{\cdot}6 \end{cases} \quad \ldots \text{(B8)}$$

$$C^{*}_{YM,bubble,front} = \begin{cases} -0{\cdot}9\,u/V\ ; & u/V \le 0{\cdot}2 \\ -0{\cdot}18 + 0{\cdot}219\left(u/V - 0{\cdot}2\right)\ ; & 0{\cdot}2 < u/V < 0{\cdot}7 \\ 0\ ; & u/V \ge 0{\cdot}7 \end{cases} \quad \ldots \text{(B9)}$$

$$\Delta C^{*}_{YM} = C^{*}_{YM,bubble,side} \times \mathrm{Cos}^{2}\left(\theta^{*}\right) + C^{*}_{YM,bubble,front} \times \mathrm{Cos}^{2}\left(\phi^{*}\right) \quad \ldots \text{(B10)}$$

As noted in section 4.2, the yawing moment model is defined by eight parameters: the basic symmetric attached flow slope (= ±0·075), the asymmetric 'coupling' slope (= +0·03), the maximum magnitude of the bubble components (= +0·07, –0·18), the normal incidences at which this maximum occurs (= 0·28, 0·20), and the upper limits of the bubble contribution (= 0·6, 0·7).

https://doi.org/10.1017/S0001924000005650 Published online by Cambridge University Press